

https://dspace.org/

Modelling the Sensitivity of the KM3NeT/ARCA and KM3NeT/ORCA to Neutrinos from Quiescent Blazars

Nkosi, Bhuti Linda

2023-09

University of the Witwatersrand, Johannesburg

https://hdl.handle.net/10539/41925

Nkosi, Bhuti Linda. (2023). Modelling the Sensitivity of the KM3NeT/ARCA and KM3NeT /ORCA to Neutrinos from Quiescent Blazars. [Master's dissertation, University of the Witwatersrand, Johannesburg]. https://hdl.handle.net/10539/41925

Downloaded from a DSpace repository. https://dspace.org/

Modelling the Sensitivity of the KM3NeT/ARCA and KM3NeT/ORCA to Neutrinos from Quiescent Blazars



WITS
UNIVERSITY

A Dissertation submitted to the Faculty of Science at the University of the Witwatersrand, Johannesburg, in fulfillment of the requirements for the degree of Master of Science in Physics.

By
Bhuti Nkosi
bhutilindankosi@outlook.com

Supervised by
Prof. Andrew Chen

Johannesburg, South Africa
December 2022

Declaration

I, Bhuti Nkosi, student number [1602018], declare that this Dissertation is my own, unaided work. It is being submitted for the Degree of Master of Science in Physics at the University of the Witwatersrand, Johannesburg. It has not been submitted before for any degree or examination at any other University.



(Signature of candidate)

4th day of **September** 20 **23** in **Johannesburg**

Abstract

Blazar jet emission has been modelled using two families of models, leptonic and hadronic, to explain the double-peaked SED. In hadronic models, the higher energy peak is explained by proton interactions with the jet material and external fields. Lepto-hadronic models are a type of blazar emission model that accounts for both leptonic and hadronic processes in the jet. In these models, the low-energy bump of the spectral energy distribution SED is produced by synchrotron radiation from primary electrons, while the high-energy bump is produced by a combination of radiation from protons and secondary particles. Lepto-hadronic models can explain the variability and spectral features of blazars in different states, such as flaring or quiescent. In this project, we used a one-zone lepto-hadronic model to simulate the blazar jet and calculate the neutrino emission and detection prospects with KM3NeT.

For Sifiso, he believed in me before I knew that I had potential. For Paul, who ensured that potential is utilized by supporting me throughout. For everyone who supported me throughout.

Acknowledgements

The financial assistance of the National Research Foundation (NRF) towards this research is hereby acknowledged, **UID 145143**. Opinions expressed and conclusions arrived at, are those of the author and are not necessarily to be attributed to the NRF.

I would like to acknowledge the National Institute for Theoretical and Computational Sciences (NITheCS) South Africa for also financially supporting this research.

I would like to acknowledge my supervisor, Prof. Andrew Chen for all the guidance and advices. I would like to acknowledge the KM3NeT Collaborators for their technical support and making this research possible.

Contents

Declaration i

Abstract ii

Dedication iii

Acknowledgements iv

List of Figures vii

List of Tables ix

1 Introduction 1

1.1 Motivation 1

1.2 Aim 2

1.3 Outline 2

2 Blazars, Neutrinos and KM3NeT 4

2.1 Blazars 4

2.1.1 Properties of blazars 5

2.1.2 Relativistic Jets 6

2.1.3 Blazar jet modelling 7

2.1.4 Quiescent Blazars 9

2.2 Invisible messengers 11

2.2.1 Introduction 11

2.2.2 Neutrinos 11

2.2.3 Properties of neutrinos 12

2.3 A new window on our Universe 14

2.3.1 Introduction 14

2.3.2 KM3NeT 14
2.3.3 KM3NeT detection technology 15

3 A closer look: OneHaLe and CALCRATE **22**
3.1 Blazar jet simulation using OneHaLe 22
3.1.1 Particle distribution evolution 23
3.1.2 Radiative evolution 28
3.2 CALCRATE 30
3.2.1 Rates 30
3.2.2 Discovery and Sensitivity 33

4 Methodology **37**
4.1 SED 37
4.2 CALCRATE methods 40
4.2.1 Rates, sensitivity and discovery 40

5 Results **43**
5.1 Results of OneHaLe 43
5.2 Results of CALCRATE 45
5.2.1 Neutrino Sensitivity, Discovery and Rates 45

6 Conclusion **50**
6.1 Summary of results 50
6.1.1 Some neutrino fluxes at the end of the tunnel 51
6.2 Main findings 52
6.3 Future work 53

List of Figures

2.1 Schematic illustration of the unified AGN model. [1] 4
2.2 From left to right, the HESS [2] and VERITAS telescopes[3] 5
2.3 Blazar jet composition and the particle interactions inside the jet.Image from [4] 6
2.4 DOM on the left, a DU in the middle and DOM being installed in the sea by the KM3NeT Collaboration.[5] 15
2.5 Configuration of the ARCA and ORCA detectors. 16
2.6 Visualization of the reconstructed tracks.[6] 18
2.7 Reconstruction of the track event from the PMTs.[6] 19

4.1 An early fit of the 3C 279 SED using the 'fit-by-eye' method ' to 3C 279 archival data found on NED. 39

5.1 SED 'fitted-by-eye' to 3C 279 archival data found on NED. Solid line represents the total neutrino flux, and the dotted lines represent neutrinos produced from the different neutrino processes. Some of the input parameters are displayed. 44
5.2 Neutrino fluxes corresponding to the SED in Figure 5.1. 44
5.3 Histogram showing MDP binned by effective energy and the viewing angle. The bin centred at (4,5) has the optimized MDP and MRF, the MDP is 644.50 and the MRF is 1649.24. 48
5.4 MRF and MDP for combined signal detected through the track and shower channel. Effective energy and the cone viewing angle are set to be at 1° and $\log E = 5$ for track events. In shower events, the effective energy and the cone viewing are set to be at 4° and $\log E = 5$ 48

5.5 Signal and background rates, for the optimized MRF and MDP for both shower and track events. Blue line is for the signal rates and the orange line is for background rates. The above plots illustrate that the source is background-dominated in all observable directions. Apparent fluctuations in the background signal are due to changes in the optimum energy threshold rather than intrinsic changes in the background or instrument sensitivity. 49

List of Tables

3.1 The functions g_0 and g_1 for ν_μ and ν_e 27

4.1 List of OneHaLe free parameters with units 38
4.2 Table showing the list of input options used for CALCRATE 40

5.1 The optimized simulated discoveries and sensitivities for a ν_μ detected using the track channel. 45
5.2 The optimized simulated discoveries and sensitivities for a ν_e detected using the track channel. 45
5.3 The optimized simulated discoveries and sensitivities for a ν_e detected using the shower channel. 45
5.4 The optimized simulated discoveries and sensitivities for a ν_μ using the shower channel. 45
5.5 The optimized simulated discoveries and sensitivities for combined ν_μ, ν_e using the track channel. 46
5.6 The optimized simulated discoveries and sensitivities for combined ν_μ, ν_e using the shower channel. 46
5.7 Simulated discoveries and sensitivities for combined ν_μ, ν_e through the shower channel. 47

6.1 Calculated upper flux limits and minimum flux needed for a discovery in each channel. The results were calculated using Equation 3.37, where $\Phi(E, \theta) = 1.75368 \times 10^{-12}$ ergs/cm^2/s for energies 10 GeV to 10^8 GeV. 51

Chapter 1

Introduction

1.1 Motivation

The detection of a high-energy neutrino by the IceCube observatory in spatial and time coincidence with a gamma-ray flare from the blazar TXS0506+056 in 2017 (event IceCube-170922A) was a breakthrough event in multi-messenger astronomy[7]. This event suggested a possible link between blazars and very high energy cosmic rays, as both gamma-rays and neutrinos could be produced by the same process: the acceleration of protons or heavier nuclei in the relativistic jets of supermassive black holes (SMBH) and their subsequent interactions with photons or matter.

One of the most promising ways to study the blazar jet environments and their variability is to use neutrino astronomy. Neutrinos are neutral and weakly interacting particles that can travel long distances without being affected by magnetic fields or radiation [8]. This means that neutrino carries the information of the environment in which they were made. Blazars are Active Galactic Nuclei (AGNs) with relativistic jets oriented in our line of sight[9]. They have a double-peaked spectral energy distribution (SED) that can be explained using two different types of models, the hadronic models and the leptonic models. In both models the lower energy peak is explained by electron synchrotron radiation. However, the higher energy peak can be explained using processes such as inverse-Compton and pair production in the case of leptonic models, but for hadronic models the higher energy peak is explained in terms of proton synchrotron and other proton processes[9].

The hadronic models predict that blazars can produce high-energy neutrinos through

interactions of protons with photons or matter in the jet. These neutrinos can be detected by telescopes, which uses a large volume of ice or water as a target for neutrino interactions. By measuring the direction, energy and flavor of the neutrinos, we can identify neutrino sources and test the hadronic model. On the other hand, the leptonic models do not predict significant neutrino emission from blazars, as electrons do not produce neutrinos directly. Therefore, neutrino detection from non-flaring blazars can help to discriminate between the two models and constrain the physical parameters of the blazar jets, such as magnetic field strength, jet power and particle acceleration mechanisms.

1.2 Aim

The detection of neutrinos from blazars in non-flaring state is a challenging but rewarding task for astrophysics. Non-flaring blazar flares are less luminous and more difficult to detect and measure their spectra.

The goal of this project is to investigate the detectability of neutrinos from blazars in quiescent state with the KM3NeT/ARCA. KM3NeT/ARCA is a large-scale underwater neutrino telescope under construction in the Mediterranean Sea, which will have a high sensitivity to neutrinos in the TeV-PeV range[10]. By using a multi-messenger approach that combines multiwavelength electromagnetic data and neutrino data, we aim to constrain the hadronic models of blazar emission and test the hypothesis that blazars are neutrino accelerators.

1.3 Outline

The structure of this dissertation is as follows. Chapter 2 provides a comprehensive overview of the theoretical framework that underpins this research, including the relevant concepts and equations of relativistic astrophysics and high-energy physics. Chapter 3 introduces the lepto-hadronic model that we adopted to explain the multi-wavelength emission from blazars, and the software tool (CALCRATE, unpublished tool from KM3NeT) that we used to perform numerical simulations and data analysis. Chapter 4 introduces the approach and methodology used in this research. Chapter 5 presents the main results of this project, which include the spectral modeling of several blazar sources, the parameter estimation and uncertainty analysis, and the comparison with other models and observations. Chapter 6 discusses the implications and limitations of our findings, and offers some suggestions for future

work in this field.

Chapter 2

Blazars, Neutrinos and KM3NeT

2.1 Blazars

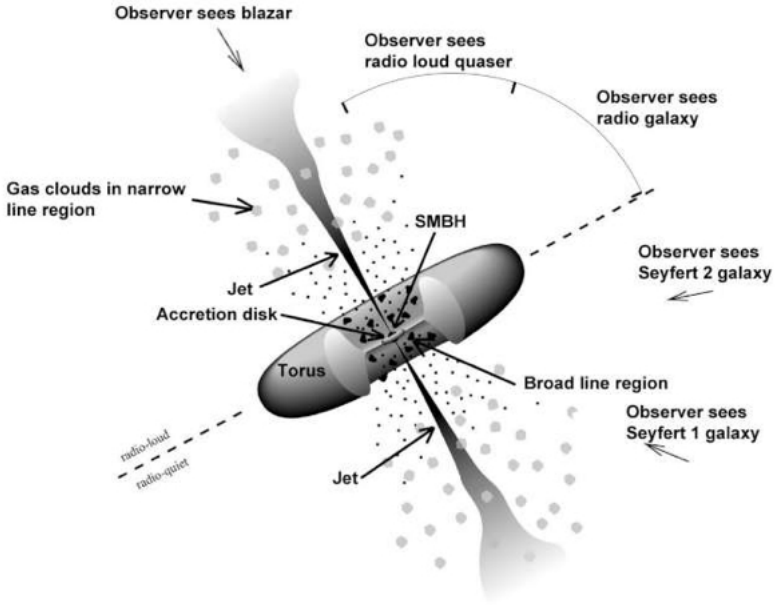

Figure 2.1: Schematic illustration of the unified AGN model. [1]

Blazars are a fascinating and unique category of celestial objects that have captured the attention of astronomers in recent decades. These objects are a subcategory of AGN, which are galaxies that contain a central SMBH that emits significant amounts of radiation. However, blazars are distinguished by their unusually strong emission of high-energy gamma-ray radiation, which makes them some of the brightest objects in the sky. Blazars also exhibit other unusual characteristics that make them

particularly interesting. For example, they can vary significantly in brightness over relatively short periods of time, sometimes fluctuating by factors of 10 or more in just a few hours. This variability is not well understood.[11]

Blazars are also notable for their large redshifts, which indicate that they are located very far away. This makes them important tools for cosmologists to study the early universe, as the distant blazars allow us to look back in time and observe the conditions of the host galaxy when the light we see was emitted. There are a number of theories about how blazars form and what powers their intense radiation. Most models suggest interactions inside the jet; only the radio emission has substantial contribution from the intergalactic medium. [12]

The study of blazars is an active area of research in astronomy, with many telescopes and observatories dedicated to observing and studying these fascinating objects. The Fermi Gamma-Ray Space Telescope[13], for example, is a satellite-based observatory that has been designed to search for blazars and other sources of high-energy gamma-ray emissions. On the ground, telescopes like the Very Energetic Radiation Imaging Telescope Array System (VERITAS)[3] and the High Energy Stereoscopic System (HESS)[2] are also used to study the properties of blazars.[14]

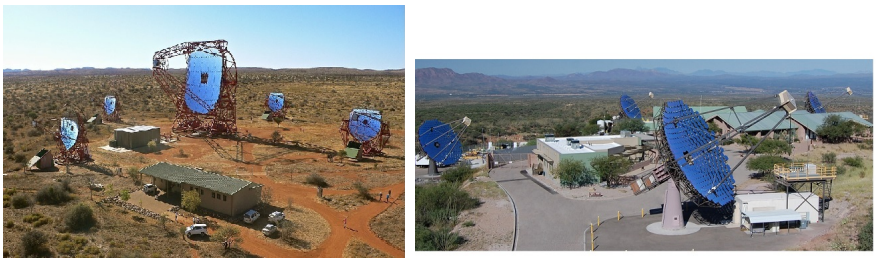

Figure 2.2: From left to right, the HESS [2] and VERITAS telescopes[3]

Overall, blazars are some of the most intriguing and unique objects in the universe, offering a valuable window into the early history of the cosmos and the physics of extreme phenomena like black holes and relativistic particle jets.

2.1.1 Properties of blazars

Here are some of the properties of blazars:

- High Luminosity: One of the key properties of blazars is their high luminosity, which can range from 10^{43} to 10^{47} erg/s in γ-rays. This is often attributed to relativistic beaming of the jet material in our line of sight.[15]

- Jets: Blazars are also characterized by highly collimated and relativistic jets of plasma, which are powered by the same black hole accretion process. These jets can extend up to several millions of light-years in distance and emit radiation across the electromagnetic spectrum.[16, 17]

- Variability: Blazars exhibit rapid and unpredictable variations in their brightness levels, especially in the gamma-ray and X-ray bands. This variability is thought to be linked to instabilities in the accretion disk and jet, as well as to changes in the properties of the surrounding gas and dust[18]. It can also be associated with changes in the viewing angle of the emitting region[19], these changes in the viewing angles affects the apparent fluxes observed and the variability time scales. This can be explain by using Doppler boosting.

- Polarization: Another unique property of blazars is the high degree of polarization in their radiation, especially in the optical band. This is believed to result from the intense magnetic fields that are generated by the jet plasma.[9]

Blazars are likely to be sources of multimessenger emission, which means they produce radiation across multiple wavelengths and also emit high-energy neutrinos (e.g. TXS0506+056) and cosmic rays. This makes them important targets for astronomy and astroparticle physics studies.[7, 17, 20]

2.1.2 Relativistic Jets

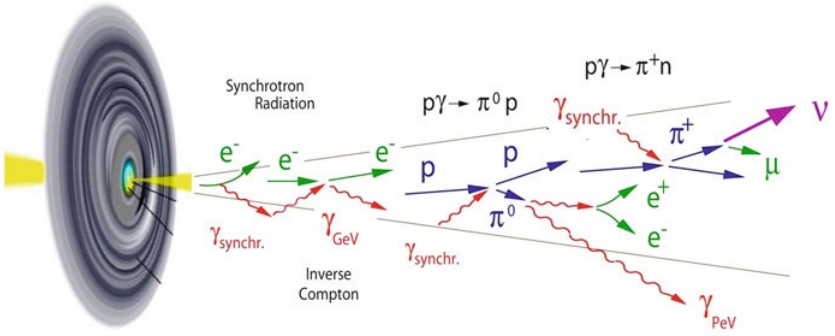

Figure 2.3: Blazar jet composition and the particle interactions inside the jet.Image from [4]

Blazar spectra are dominated by non-thermal emission, with a double-peaked SED with one in the lower energies (radio to soft X-ray) and one in the X-ray to gamma-ray regime or higher energies. This highly variable gamma-ray emission makes blazars a valuable tool in studying high-energy astrophysics.[21, 22, 23]

In addition to their high-energy emission, blazars have also been observed in other bands of the electromagnetic spectrum, including radio, optical, and X-ray. These observations have enabled the study of the structure and evolution of these objects in detail and have provided important insights into the physics of active galactic nuclei and the growth of supermassive black holes. Blazars can be classified using two subcategories, BL Lacs (BL Lacertae objects) and FSRQ (flat-spectrum radio quasars). However, they have distinct characteristics that differentiate them.

BL Lacs are characterized by their absence of defined emission lines in their optical spectra, indicating a lack of hot material in their vicinity. This implies that BL Lacs are almost "naked" black holes, with little or no surrounding gas or dust. FSRQs, on the other hand, have prominent spectral lines in their emissions, indicating the presence of gas and dust in the vicinity of the central black hole. They peak in the MeV-GeV range rather than the GeV-TeV range.[24]

In summary, BL Lacs are characterized by lack of prominent emission lines, while FSRQs have clear spectral lines.[24]

2.1.3 Blazar jet modelling

Two competing types of models, leptonic and hadronic, are commonly used to explain the origin of the observed emission from blazars.

Leptonic models:

The leptonic models assume that the non-thermal radiation from blazars arises from the acceleration and synchrotron emission of high-energy electrons in a relativistic jet. The electrons lose energy through inverse Compton scattering with photons in the jet, resulting in high-energy gamma-ray emission. This model can explain the observed spectral energy distribution of blazars, which typically exhibits a peak in the range of gamma-rays.[9, 25, 26, 12]

Hadronic models:

The hadronic models, on the other hand, assume that the non-thermal emission is due to the interactions of high-energy protons in the jet. These protons interact with photons or matter in the jet, producing charged pions that eventually decay into gamma-rays. This model can explain the low-frequency radio emission observed in some blazars, which cannot be easily explained by the leptonic model.[9, 25, 26, 12]

Both models have their strengths and weaknesses and have been applied to different sources depending on the observed properties. However, a growing body of evidence suggests that both mechanisms may be operating simultaneously, making it difficult to distinguish between them [22, 9]. This is called the lepto-hadronic model. In these models, it is assumed that both ultrarelativistic electrons and ultrarelativistic protons are present in the jet material and both contributes a similar (in theory) amount to the fluxes. The presence of ultrarelativistic protons mean that the interactions inside the jet include proton-induced electromagnetic (EM) cascades, neutral pion decay, Bethe-Heitler (BH) pair production and proton synchrotron radiation[25]. The interaction of protons with the jet material and target photons can lead to photopion interactions. Photopion interactions can happen in two basic channels:

(a) $p + \gamma \rightarrow p + \pi^0$

(b) $p + \gamma \rightarrow n + \pi^+$

which are equally probable. The neutrons can either escape the jet emission region or interact with the target photons leading to the following interactions, which are also equally probable

(c) $n + \gamma \rightarrow n + \pi^0$

(d) $n + \gamma \rightarrow n + \pi^-$.

The neutrons can also decay into protons with a half-life of $\tau = 881.5 \pm 1.5s$

(e) $n \rightarrow p + e^- + \bar{\nu}_e$.

Following the photopion production, pion decay and muon decay can occur to produce neutrinos; these processes are defined by the following equations
(f) $\pi^\pm \rightarrow \mu^\pm + \nu_\mu(\bar{\nu_\mu})$ for pion decay

(g) $\mu^\pm \rightarrow e^\pm + \bar{\nu_\mu}(\nu_\mu) + \nu_e(\bar{\nu_e})$ for muon decay.

The electrons (positrons), muons, protons and pions (charged) can undergo synchrotron radiation to produce γ-rays which will then escape the jet emission region. Furthermore, the electrons can interact with positrons to create γ-rays. Neutral

pions will decay into γ-rays. BH pair production also increases the population of electrons; the interaction process is given as follows:

(h) $p + \gamma \rightarrow p' + e^+ + e^-$, where p' is the proton in the lab frame.

Photons and neutrinos escape, with neutrinos having little to no interactions, hence carrying the information about the environment in which they were created.[9, 25, 26, 12]

2.1.4 Quiescent Blazars

When a blazar is in a quiescent or non-flaring state, the blazar exhibits little to no flares in fluxes over the period of observation[27]. A blazar would normally remain in that state for an extended period of time that could go to up to years, then suddenly have a huge increase in the flux that could be by factors of more than 100. This sudden increase could go to time-scales of several years, 3.5 years in the case of S5 1803+ 78 [28], from a time-scale of less than an hour, around 33 minutes in the case of NRAO 530 [29]. This makes it hard to explain what causes blazar flares due to varying time-scales. In the absence of neutrinos from a flaring blazar, both leptonic and hadronic models can be used to explain the observed spectra. However, if neutrinos coincides with the blazar flare spatially and in time, hadronic models are favoured over the purely leptonic models. After the flare, the blazar could go back to the initial non-flaring state or obtain a new non-flaring state. With everything considered, explaining the flare becomes a troublesome task, since the two types of blazar jet models used imply different blazar environmental conditions[22]. We then need to constrain the types of models that could be used so that a blazar emission mechanism can be fully understood.

Here is what makes observations of blazars in quiescent state very important:

- Blazars can remain in non-flaring state for a long time, which allows for longer studies of a source.

- Observational data from non-flaring blazars can be used to characterize and classify blazars.

- Some studies suggest that the flare could be due to external factors[30] and others changes in the inter jet environment[31], so studying quiescent blazars

could help understand the environment surrounding the blazar.

Detection of neutrinos from blazars in quiescent state would suggest that blazars fundamentally have substantial contribution from protons/neutrons even without a flare. This would rule out the purely leptonic models when fitting observed spectra, and use either lepto-hadronic models which are slightly dominated by leptonic interactions over hadronic interactions or models which are dominated by hadronic processes. Since neutrinos weakly interacts with matter, they are more likely to contain information such as the energy and direction of the location where they were created. We can use that information together with multi-messenger observations of the same source to find the distance from the SMBH in which the jet was collimated and the initial conditions in which neutrinos were made.

2.2 Invisible messengers

2.2.1 Introduction

Neutrinos are subatomic particles with no electrical charge and very low mass. These ghostly particles are difficult to detect because they interact very weakly with matter, which makes them travel through the universe almost completely unimpeded. First proposed by Wolfgang Pauli in 1930[8], neutrinos were discovered in 1956 by Clyde Cowan and Frederick Reines, for which they were awarded the 1995 Nobel Prize in Physics. Since then, neutrinos have become the subject of intense research, not only because of their elusive nature, but also because they offer valuable insights into the properties of matter and the structure of the universe.

2.2.2 Neutrinos

Neutrinos are elementary particles. There are three types of neutrinos known as electron neutrino, muon neutrino, and tau neutrino. According to the Standard Model of particle physics, each type of neutrino is associated with a charged particle: electron neutrinos are emitted during beta decay, muon neutrinos are produced when muons decay, and tau neutrinos are generated when tau leptons decay. Neutrinos have no electric charge and very little mass, which means they are almost as massless as a photon[7]. In fact, neutrinos were long thought to be massless, but experiments conducted in the late 1990s and early 2000s have shown that they do have mass, albeit very small. These experiments also showed that neutrinos have the unique property of oscillation, which means they can change from one type to another as they travel through space[32].

Neutrinos are notoriously difficult to detect because of their feeble interactions with matter. Neutrinos can pass through dense materials like lead, concrete, and even the entire Earth with minimal disruption. However, when a neutrino does interact with matter, it can produce a secondary particle that can be detected. There are several methods used to detect neutrinos, such as the Cherenkov radiation, scintillation, and liquid argon detectors. The Cherenkov radiation method involves measuring the flashes of light produced when a neutrino interacts with water or ice, and the charged particles produced by the neutrino interactions travel faster than the speed of light in the medium[33]. The scintillation method uses materials like organic liquid scintillators, which emit photons when a neutrino interacts with it. The liquid argon detector uses liquid argon as the detection medium that uses the ionization energy

by the neutrinos to produce a signal.[14]

Neutrinos have played a significant role in astrophysics and particle physics. Neutrinos have been detected from several natural sources, such as the Sun[34], supernovae, and AGN, with prospects of detection in gamma-ray bursts[35]. These detections provide insights into the stellar phenomena, nuclear reactions, and the evolution of the universe itself. Neutrinos have also contributed to our understanding of the structure of matter. In 1983, the discovery of the W and Z bosons at CERN's proton-antiproton collider, made possible through the indirect detection of neutrinos using momentum conservation, confirmed the electroweak theory that unified the electromagnetic and weak forces[36]. The discovery of neutrino oscillation in 1998 demonstrates that neutrinos have mass and that the Standard Model must be extended to explain their behavior[37].

2.2.3 Properties of neutrinos

The properties of neutrinos can be summarized as follows[38]

- Neutrinos have very little mass: Neutrinos are one of the lightest known particles in the universe. Their mass is on the order of 10^{-35} kg, which is less than a millionth of the mass of an electron.

- Neutrinos are electrically neutral: Unlike protons, electrons, and other particles that have electric charge, neutrinos are electrically neutral. They do not interact with electromagnetic forces and cannot be deflected by magnetic fields.

- Neutrinos are able to travel great distances: Neutrinos are able to travel through matter with very little interaction, making them able to travel great distances through space. This allows them to be detected from sources many light-years away.

- Neutrinos have three different types or flavors: Neutrinos come in three different flavors: electron neutrinos, muon neutrinos, and tau neutrinos. They can change from one flavor to another, a phenomenon known as neutrino oscillation.

- Neutrinos are extremely abundant: Neutrinos are one of the most abundant particles in the universe. It is estimated that more than a trillion neutrinos

pass through a human body every second.

- Neutrinos are produced in a variety of astrophysical processes: Neutrinos are produced in many astrophysical processes, such as nuclear reactions in stars, supernova explosions, and black hole accretion disks.

- Neutrinos may have played a role in the evolution of the universe: Neutrinos may have played an important role in the evolution of the universe, helping to drive processes such as nucleosynthesis and even the formation of galaxies.

Neutrinos are an essential particle in particle physics and astrophysics. Their properties of small mass, zero electric charge, and weak interactions with matter make them challenging to detect, but their detection has contributed significantly to our understanding of the universe's structure and the behavior of matter. [39]

2.3 A new window on our Universe

2.3.1 Introduction

Neutrino astronomy is an emerging field of study that aims to detect and observe neutrinos emitted by astrophysical sources in space. These include supernovae, gamma-ray bursts, and black holes, among others. In recent years, numerous neutrino observatories have been established around the world to study these elusive particles, including the IceCube observatory in Antarctica and the Super-Kamiokande observatory in Japan[14, 40]. However, none of these facilities can match the angular resolution of the KM3NeT[41] underwater neutrino observatory, which promises to revolutionize the field of neutrino astronomy alongside IceCube-Gen2[42].

2.3.2 KM3NeT

KM3NeT (Kilometer Cube Neutrino Telescope) is a multi-national research consortium that aims to construct a kilometers-scale neutrino detector of unprecedented sensitivity for the study of astrophysical neutrino sources. The observatory will be built at the bottom of the Mediterranean Sea, at depths ranging from 2 to 4 km. The KM3NeT has two main detectors, namely: ARCA and ORCA. ARCA is an acronym for Astroparticle Research with Cosmics in the Abyss and ORCA is an acronym for Oscillation Research with Cosmics in the Abyss. The detection units of the ARCA telescope will be anchored at a depth of about 3500 m and ORCA around 2500 m.[41, 43, 10]

The main scientific objectives of the KM3NeT project are to[41]:

- Study the sources and properties of cosmic neutrinos with energies up to several PeV.
- Search for new and exotic astrophysical phenomena, such as dark matter, magnetic monopoles, and cosmic rays.
- Study the properties of neutrinos themselves, including their mass, mixing, and oscillation patterns.

The KM3NeT observatory is expected to have a profound impact on the field of neutrino astronomy and astrophysics. The ability to detect and study high-energy neutrinos with unprecedented sensitivity will allow exploration of the properties and

sources of these elusive particles and advance our understanding of the universe. The observatory will also serve as a platform for testing and advancing the technology and techniques used in the detection of neutrinos, paving the way for future innovations in the field. By advancing our understanding of neutrinos and their sources, KM3NeT will make significant contributions to the fields of astrophysics, particle physics, and cosmology.

2.3.3 KM3NeT detection technology

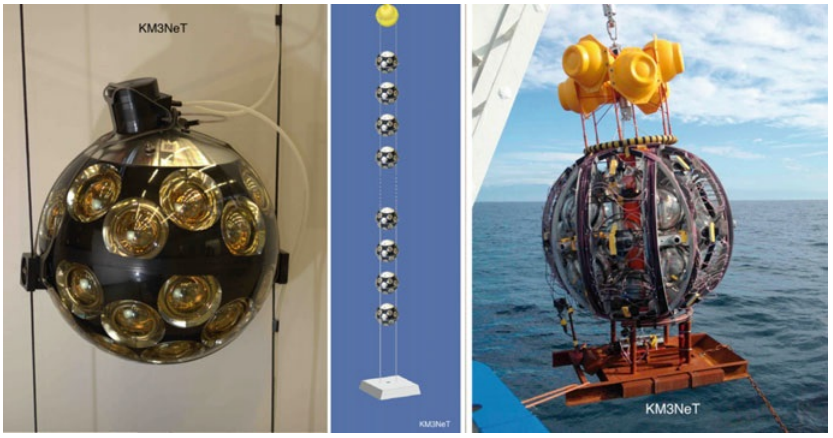

Figure 2.4: DOM on the left, a DU in the middle and DOM being installed in the sea by the KM3NeT Collaboration.[5]

The ARCA and ORCA telescopes consist of vertical strings of light sensors, called detection units (DUs), that are anchored to the seabed and connected to shore stations by cables. Each DU has 18 digital optical modules (DOMs) that contain 31 photo-multiplier tubes (PMTs) each. The PMTs amplify and record the faint flashes of Cherenkov light that are emitted by charged particles produced in neutrino interactions with the water molecules.[5]

The ARCA telescope will have two detector blocks, each consisting of 115 vertical detection units (in total 230 DUs) that are about 700 m high and equipped with light sensor modules, see Figure 2.5. These modules will detect the faint Cherenkov light produced by the charged particles from neutrino interactions inside or near the telescope. The ARCA telescope will use its high angular resolution to study the cosmic neutrino flux and its properties, such as origin, energy spectrum and flavour composition. The ARCA telescope will also map 87% of the sky, including most of the Galaxy and the Galactic Center, where some unexplained phenomena have been observed by other astroparticle detectors. The low scattering of the sea water will allow precise measurement of the neutrino direction, which is crucial for identifying

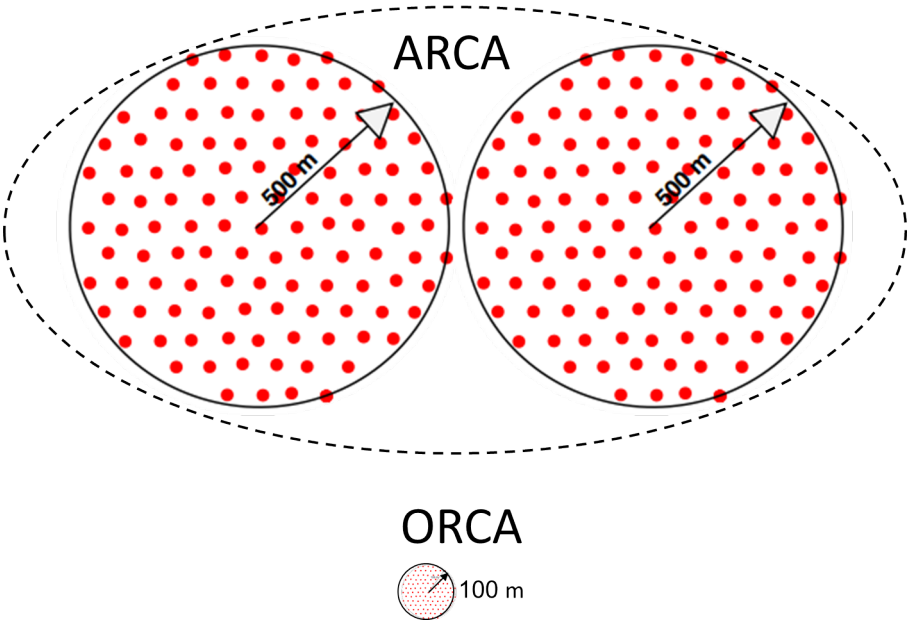

Figure 2.5: Configuration of the ARCA and ORCA detectors.

the sources of these elusive particles[43], as well as confirming previously discovered sources including NGC1068[44] and TXS0506+056[7].

The ORCA detector uses the high flux of atmospheric neutrinos, which are created by cosmic rays interacting with the Earth's atmosphere, to probe the fundamental properties of these elusive particles. One of the main goals of ORCA is to determine the neutrino mass hierarchy, which is the unknown ordering of the three neutrino mass eigenstates. This can be done by studying how neutrinos change their flavour as they travel through matter, a phenomenon known as neutrino oscillation. The neutrino mass hierarchy affects the oscillation patterns of different neutrino flavours as a function of their energy and path length through the Earth. By measuring these patterns with high precision, ORCA can reveal the nature of the neutrino mass spectrum.[45]

Event reconstruction

The reconstruction of neutrino events in KM3NeT involves several steps. The first step is to identify the hits or signals produced by the PMTs in each optical module. This is done by applying suitable filters that remove noise and other spurious signals. Then, the time and charge information for each hit is recorded and sent to a central data processing unit (DPU), where the event reconstruction takes place.

The goal of the event reconstruction algorithms is to infer the neutrino's path and

energy from the hits recorded by all the optical modules that were activated by the same neutrino interaction. This is a challenging task because the number of hits can be very large and the neutrino energy is not known beforehand. Some of the most commonly used algorithms include the likelihood fit method. These algorithms take into account various factors such as the arrival time of the neutrino, the direction and length of the muon track (if a muon was produced), and the spatial distribution of the hits in the detector. Shower events are reconstructed using the energy of the shower and the angular size of the shower.

Once the event reconstruction is complete, the resulting data is analyzed and compared with theoretical models to extract useful information about the properties of neutrinos and their sources. This information can help us better understand the mysteries of the universe and the nature of the fundamental particles that make it up.

Cherenkov radiation

A type of electromagnetic radiation called Cherenkov radiation is emitted when a medium is traversed by a charged particle that moves faster than the speed of light in that medium. The radiation forms a shockwave in the shape of a cone along the path of the particle. The color and brightness of the radiation are determined by the particle's energy and speed, as well as the medium's refractive index. In nuclear reactors, Cherenkov radiation causes a blue glow in the water around the fuel rods. Cherenkov radiation has various applications, such as detecting high-energy particles, studying the characteristics of cosmic rays, and imaging biological tissues.[33]

When a charged particle (such as an electron) travels faster than light in a certain medium (such as water) with a refractive index n, the atoms in the medium get disturbed and release photons in a form of a shock wave of visible light. This light is usually blue because the photons released have high frequencies and short wavelengths. The angle θ_C between the direction of the particle and the direction of the photon emission depends on n and the speed of the particle v, and it can be calculated by

$$\cos\theta_C = \frac{1}{\beta n} \tag{2.1}$$

where $\beta = v/c$ and c is the speed of light in vacuum. The number of Cherenkov photons N that a particle with charge Ze emits per unit wavelength interval $d\lambda$ and

per unit distance travelled dx, is given by:

$$\frac{d^2N}{dxd\lambda} = \frac{2\pi\alpha z^2}{\lambda^2}\left(1 - \frac{1}{\beta^2 n^2(\lambda)}\right) \tag{2.2}$$

where λ is the wavelength of the photon and α is the fine structure constant. In water, which is transparent from 300 nm to 600 nm in wavelength, this results in a blue or violet glow that can be seen in some nuclear reactors. Cherenkov radiation is used to detect high-energy charged particles and cosmic rays or gamma rays.

Track reconstruction

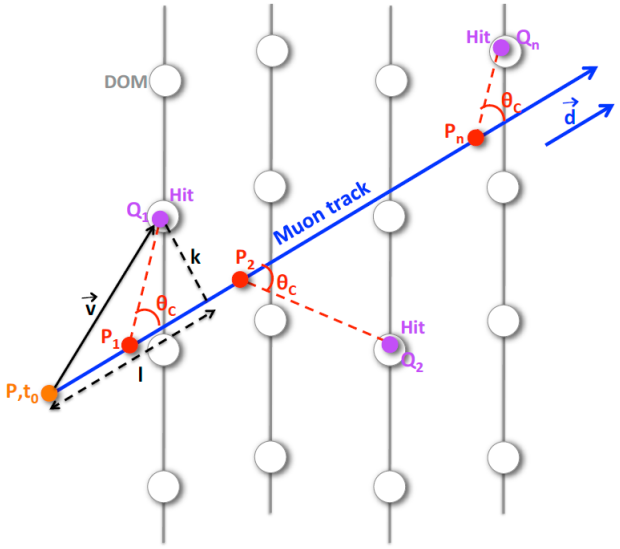

Figure 2.6: Visualization of the reconstructed tracks.[6]

We consider muons with energies above $E_\mu \gtrsim 100$ GeV that can pass through the detectors, since the atmospheric muon fluxes are low at those energies. The effects of multiple scattering and finite energy on the muon trajectory and velocity are small enough to be neglected. The muon position at a given time t_0 is denoted by

$$\vec{P} \equiv (p_x, p_y, p_z)$$

and its normalized direction is given by

$$\vec{d} \equiv (d_x, d_y, d_z)$$

, which can be written in terms of the polar and azimuthal angles θ and ϕ as

$$\vec{d} \equiv (\sin\theta\cos\phi, \sin\theta\sin\phi, \cos\theta).$$

The goal of the reconstruction algorithm is to estimate the five parameters $p_x, p_y, p_z, \theta, \phi$ and a quality parameter for the quality of the track fit that can be used to discard events with poor reconstruction. The muon energy is not directly calculated by any algorithm, but for the analysis on point-like sources, the number of selected hits is used as a proxy for the energy. A key quantity used in the reconstruction is the so-called "time residual", which is the difference between the actual hit time t_i and the expected time of arrival t_{th} of the photon on the PMT. The time residual is computed assuming that the event starts at a time t_0, the muon follows a straight line with speed c and the Cherenkov light is produced at a Cherenkov angle $\theta_C \sim 42°$ relative to the muon direction with a speed c/n, where n is the refractive index in the medium (n $\sim$ 1.35) Figure 2.7 illustrates the track description used in the reconstruction. Let $\vec{v}$ be the vector from the point $\vec{P}$ to the hit position $\vec{Q}_i$, i.e.

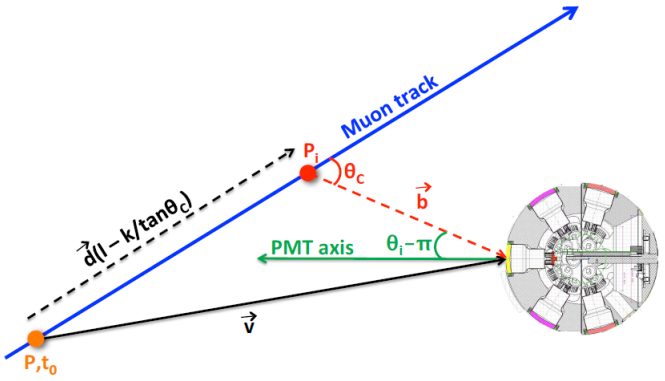

Figure 2.7: Reconstruction of the track event from the PMTs.[6]

$\vec{v} = \vec{Q}_i - \vec{P}$, where a photon reaches a PMT. We can decompose $\vec{v}$ into two components: l, which is the projection of $\vec{v}$ onto the muon direction $\vec{d}$, and k, which is the length of the vector perpendicular to $\vec{d}$. Then we have $l = \vec{v} \cdot \vec{d}$ and $k = \sqrt{|\vec{v}|^2 - l^2}$. The photon is emitted at a point $\vec{P}_e$ along the muon track, such that

$$\vec{P_e} = l - \frac{k}{\tan\theta_C} \tag{2.3}$$

where θ_C is the Cherenkov angle. The photon travels a distance of

$$b = \frac{k}{\sin\theta_C} \tag{2.4}$$

to reach the PMT. The theoretical arrival time of the photon at $\vec{Q}_i$ is then

$$t^{th} = t_0 + \frac{1}{c}\left(l - \frac{k}{\tan\theta_C}\right) + \frac{n}{c}\left(\frac{k}{\sin\theta_C}\right) \tag{2.5}$$

where t_0 is the time of emission of the muon, c is the speed of light in vacuum and n is the refractive index of water. Given the measured time t_i and position $\vec{Q}_i$ of each hit, we can define the time residual $r_i = t_i - t_i^{th}$, which depends only on $\vec{P}$ and $\vec{d}$. Another relevant quantity is the expected angle of incidence θ_i of the photon on the PMT, which is the angle between the photon direction and the normalised direction, $\vec{w}$, of the PMT axis. Assuming that the photon is emitted at θ_C, setting $\vec{s} = \left[\vec{v} - \vec{d}\left(l - \frac{k}{\tan\theta_C}\right)\right]$ we can compute $\cos\theta_i$ as

$$\cos\theta_i = \frac{1}{|s|}\left(\vec{s}\cdot\vec{w}\right) \tag{2.6}$$

using the above equation we can then find θ_i which is the direction from which the signal originates. Combining signals from multiple points along the muon track, the muon track direction can then be determined.

Background sources

One of the challenges of detecting neutrino signals is to reduce the background noise from other sources of radiation. There are three main optical background sources, bioluminescence,^{40}K decay, and atmospheric muons/neutrinos. Bioluminescence is the emission of light by living organisms in the deep sea, which can interfere with the detection of faint scintillation signals from neutrino interactions[46]. ^{40}K decay is the radioactive decay of potassium-40, a naturally occurring isotope that is present in seawater and in some materials used to construct the detector. Atmospheric muons/neutrinos are high-energy particles that are produced by cosmic rays hitting the upper atmosphere and can penetrate deep into the ocean, mimicking cosmic signals or creating secondary particles that can trigger the detector. These optical background sources pose a significant challenge for KM3NeT and require careful analysis and mitigation strategies.[47, 5, 43]

One of the ways to reduce the background noise from bioluminescence is to use a time-coincidence technique, which requires that two or more optical modules detect a signal within a short time window to be considered as a valid event. This reduces the chance of false positives from single flashes of light that are not related to neutrino interactions. Another way to reduce the background noise from ^{40}K decay is to use a pulse-shape discrimination technique, which exploits the difference in the shape of the scintillation signals from ^{40}K decay and neutrino interactions. The signals from ^{40}K decay have a faster rise and fall time than the signals from

neutrino interactions, which allows them to be distinguished and rejected by applying a threshold on the pulse-shape parameter. Finally, one of the ways to reduce the background noise from atmospheric muons/neutrinos is to use a directional reconstruction technique, which uses the information from multiple optical modules to determine the direction of the incoming particle. This allows them to discriminate between upward-going neutrinos that originate from astrophysical sources and downward-going muons/neutrinos that originate from cosmic rays. We are also left with upward-going atmospheric neutrinos.[47, 5, 43]

Chapter 3

A closer look: OneHaLe and CALCRATE

In this chapter, we present a simulation study of neutrino detection from a blazar with the KM3NeT telescope. We used a time-dependent lepto-hadronic model, called OneHaLe[25], to generate neutrino fluxes from a representative source, 3C279, whose multiwavelength spectral data was obtained from the NASA Extragalactic Database (NED)[48]. We then applied CALCRATE, a tool that computes expected rates, sensitivities and discovery potentials for neutrino telescopes, using detector response functions and fluxes as inputs. This simulation allowed us to estimate the performance of KM3NeT in detecting neutrino events from 3C279 and other similar sources.

3.1 Blazar jet simulation using OneHaLe

In this section, we present OneHaLe, a code developed by M. Zacharias that is described in detail in [25],[26] and [12]. Here, we only give a brief overview of the main features and assumptions of OneHaLe, as a detailed discussion is beyond the scope of this study. OneHaLe assumes that protons and electrons/positrons originate from the same location and are accelerated by a uniform magnetic field co-moving with the jet. The primary particles then interact with the magnetic field and external photon fields to produce secondary particles, such as $e^{\pm}$, $\mu^{\pm}$, $\pi^{\pm}$, π^{0}, photons and ν. The electrons and protons do not interact with each other in the emission region.

We then discuss the key assumptions and calculations involved in OneHaLe, including the geometry, the bulk flow of particles and fields (radiation and magnetic fields), and the particle distributions after the interactions with external photon fields, synchrotron photon fields and magnetic fields are solved using the Fokker-Planck equation. We adopt the cosmology with $\Omega_m = 0.3$, $\Omega_\Lambda = 0.7$ and $H_0 = 70$ km.s^{-1}.Mpc^{-1}.

3.1.1 Particle distribution evolution

A spherical region with a radius R and a distance $z_0 = 6GM_0/c^2$ from a SMBH with mass M_0 emits protons and electrons. The region moves with a constant bulk Lorentz factor Γ and an angle θ^{obs} relative to the observer's line of sight. The Doppler factor can be expressed as,

$$\delta = \frac{1}{\Gamma\left(1 - \beta_\Gamma \cos\theta^{obs}\right)} \tag{3.1}$$

where $\beta_\Gamma = \sqrt{1 - \Gamma^{-1}}$. The particles interact with both external and internal radiation fields and magnetic fields with strength B.

The Fokker-Planck equations for protons, electrons, pions and muons describe how the particle distribution changes with time t. The Fokker-Planck equation is

$$\frac{\partial n_i(\chi,t)}{\partial t} = \frac{\partial}{\partial \chi}\left[\frac{\chi^2}{(a+2)t_{acc}}\frac{\partial n_i(\chi,t)}{\partial \chi}\right] - \frac{\partial}{\partial \chi}(\dot{\chi}_i n_i(\chi,t)) + Q_i(\chi) - \frac{n_i(\chi,t)}{t_{esc}} - \frac{n_i(\chi,t)}{\gamma t^*_{i,decay}} \tag{3.2}$$

where $\chi = \gamma\beta$ is the normalized momentum. Subscript i represents the particle species mentioned above. The particle density is n_i, a ratio of the shock to Alfvèn speed, $t_{acc}(t) = \eta_{acc} t_{esc}(t)$ is the time-scale for energy-independent re-acceleration of particles in the acceleration zone, momentum gain and loss rate is given by $\dot{\chi}_i = |\dot{\chi}_{i,loss}| - \dot{\chi}_{acc}$ where the acceleration rate is parametrized as,

$$\dot{\chi}_{acc} = \frac{\chi}{t_{acc}} \tag{3.3}$$

$t^*_{i,decay}$ is the decay time-scale of the unstable particles in their rest frame and $t_{esc}(t) = \eta_{esc} R(t)/c$ is the time-scale in which a particle escapes the emission region. $Q_i(\chi)$ is the particle injection rate.

OneHaLe considers a scenario where electrons and protons are injected with a power law spectrum in a region of size R as primary particles. These particles are pre-

accelerated and interact with various fields, such as magnetic fields and external photon fields. These interactions produce secondary particles. The injection rate of the secondary particles depends on the process that created them. We can write the primary injection rate as

$$Q_i(\gamma) = Q_{i,0}\gamma^{-q_i} H(\gamma; \gamma_{min}, \gamma_{max}) = Q_{i,0}\chi^{-q_i} H(\chi; \chi_{min}, \chi_{max}) = Q_i(\chi) \tag{3.4}$$

where γ is the Lorentz factor of the particle, q_i is the spectral index, and H is the Heaviside function defined by

$$H(\chi; \chi_{min}, \chi_{max}) = H(\gamma; \gamma_{min}, \gamma_{max}) = \begin{cases} 1, & \text{if } \gamma_{min} \leq \gamma \leq \gamma_{max} \\ 0, & \text{otherwise} \end{cases}$$

The normalization constants $Q_{p,0}$ and $Q_{e,0}$ are determined by the injection luminosity of protons and electrons ($L_{p,inj}$ and $L_{e,inj}$), the total energy density, and the Eddington luminosity, L_{Edd}. See Zacharias[25]

The sources of photons in the AGN jet are synchrotron radiation of electrons and protons, and the primary particles interacting with the fields present in the jet. Protons interact with the internal and external radiation to produce secondary particles, such as muons, pions, electrons and photons. Secondary electrons are created by Bethe-Heitler pair production (BH pair production), when a photon and a proton collide. The photons are created by synchrotron radiation of the secondary electrons and protons, and inverse Compton processes such as Synchrotron Self-Compton (SSC). The charged pions decay into muons, which then decay into neutrinos, while the neutral pions decay into two photons.

Evolution of protons

The target fields in the jet environment cause protons to lose their momentum as they interact with them. The magnetic fields also affect the protons via synchrotron cooling. The magnetic density is given by $u_B = B^2/8\pi$. The protons can also interact with radiation fields via BH pair production and pion production. Another way that protons lose their momentum is through the adiabatic process. Since we are studying blazars in quiescent state, the adiabatic processes contribution are not that significant. The terms for the momentum loss rates, $\dot{\chi}_{p,loss}$ or $-\dot{\chi}_{p,loss}$, are as follows[25]:

$$-\dot{\chi}_{p,syn} = \frac{4c\sigma_T}{3m_e c^2} u_B \left(\frac{m_e}{m_p}\right)^3 \chi^2 \tag{3.5}$$

for synchrotron cooling,

$$-\dot{\chi}_{p,adi} = \frac{3c\tan(\eta_0/\Gamma)}{R}\left(\gamma - \gamma^{-1}\right) \tag{3.6}$$

for adiabatic cooling,

$$-\dot{\chi}_{p,BH} = \alpha_S r_e^2 c \frac{m_e}{m_p} \int_2^\infty d\kappa\, n_{ph}(\frac{\kappa}{2\gamma}) \frac{\Phi(\kappa)}{\kappa^2} \tag{3.7}$$

for BH pair production where $\alpha_S \approx 1/137$ is the fine structure constant, $\kappa = 2\gamma\epsilon$ with $\epsilon = E_{ph}/m_e c^2$ is the normalized photon energy and r_e is the classical electron radius, η_0 is the jet opening angle (in radians), Γ is the bulk Lorentz factor and R is the distance from the central engine. The term for pion production is given in [12]. The total number of protons at any point is assumed to be not greater than the initial number of protons injected into the jet since there was no explicit consideration of neutrons, meaning that there are no interactions which convert protons into neutrons, and vice versa, so that is not considered in the model. Equation 3.2 is then solved.

Pions

Pions are the product of the photo-pion production processes, and they lose momentum via adiabatic and synchrotron cooling. To simplify the calculation of the cross-section for single pion production processes induced by neutrinos, the interaction channels (ITs) are divided into three categories. It is assumed that pions lose momentum through adiabatic and synchrotron cooling. The energy of each pion flavor i is given by $E_{\pi^i} = \sqrt{\chi^2 + 1}\, m_{\pi^i} c^2$, where m_{π^i} is the mass of the pion and χ is a dimensionless parameter. The injection rate of pions from all ITs is then given by

$$Q_{\pi^i} = m_{\pi^i} c^2 \sum_{IT} n_p(\frac{E_{\pi^i}}{\epsilon^{IT}}) \frac{m_p c^2}{E_{\pi^i}} \int_{\epsilon_{th}/2}^\infty dy\, n_{ph}(\frac{m_p c^2 y \epsilon^{IT}}{E_{\pi^i}}) M_{\pi^i}^{IT} f^{IT}(y) \tag{3.8}$$

where n_p is the proton distribution at the pion energy per each fraction of the mean energy ϵ^{IT} at each daughter particle for each IT, n_{ph} is the photon distribution, m_p is

the proton mass, $\epsilon = hv/m_e c^2$ is the normalized photon energy, $y = \sqrt{\chi_p^2 + 1}\,\epsilon$ is the integrating variable, χ_p is another dimensionless parameter, $M_{\pi^i}^{IT}$ is the multiplicity of pion production for each IT, and $f^{IT}(y)$ is a function that depends on the IT.

Neutral pions have a very short lifetime of $t^*_{\pi^0,decay} = 2.8 \times 10^{-17} s$ and they quickly decay into gamma rays. Charged pions, on the other hand, have a longer lifetime of $t_{\pi^i,decay} = 2.6 \times 10^{-8} s$ before they decay into muons and neutrinos. During this time, the pions can interact with the magnetic field and the expanding jet and lose momentum through synchrotron cooling and adiabatic process. The rate of momentum loss due to synchrotron cooling is proportional to the magnetic energy density u_B and the square of the pion momentum χ, as shown by

$$-\dot{\chi}_{\pi^i,syn} = \frac{4c\sigma_T}{3m_e c^2} u_B (\frac{m_e}{m_{\pi^i}})^3 \chi^2 \tag{3.9}$$

where c is the speed of light, σ_T is the Thompson cross section, m_e is the electron mass and m_{π^i} is the charged pion mass. The rate of momentum loss due to adiabatic process is proportional to the jet expansion speed and the Lorentz factor γ, as shown by

$$-\dot{\chi}_{\pi^i,adi} = \frac{3c\tan(\eta_0/\Gamma)}{R}(\gamma - \gamma^{-1}) \tag{3.10}$$

where η_0 is the jet opening angle (in radians), Γ is the bulk Lorentz factor and R is the distance from the central engine. The equation of motion for pions can be obtained by combining these two terms.

Muons

We can write the particle injection term for muons as

$$Q_{\mu^i} = \frac{n_{\pi^i}}{\gamma t^*_{\pi^\pm,decay}}. \tag{3.11}$$

where $n_{\pi^\pm}$ is the number density of pions and $t^*_{\pi^\pm,decay}$ is their decay time. Muons are produced by pion decay and have a lifetime of $t^*_{\mu^\pm,decay} = 2.2 \times 10^{-6} s$. They then decay into electrons, positrons and neutrinos. Muons lose momentum due to synchrotron and adiabatic processes. The rate of synchrotron cooling is

$$-\dot{\chi}_{\mu^\pm,syn} = \frac{4c\sigma_T}{3m_e c^2} u_B (\frac{m_e}{m_{\mu^\pm}})^3 \chi^2 \tag{3.12}$$

where c is the speed of light, σ_T is the Thomson cross section, m_e is the electron mass, $m_{\mu^\pm}$ is the muon mass, u_B is the magnetic energy density and χ is the Lorentz

Function	ν_μ	ν_e
$g_0(y)$	$5/3 - 3y^2 + 4y^3/3$	$2 - 6y^2 + 4y^3$
$g_1(y)$	$1/3 - 3y^2 + 8y^3/3$	$-2 + 12y - 18y^2 + 8y^3$

Table 3.1: The functions g_0 and g_1 for ν_μ and ν_e

factor. The rate of adiabatic cooling is

$$-\dot{\chi}_{\mu^\pm,adi} = \frac{3c\tan(\eta_0/\Gamma)}{R}(\gamma - \gamma^{-1}). \tag{3.13}$$

We can solve equation 3.2 for muons using these rates.

Neutrinos

Muon neutrinos are created from pion decay. Electron neutrinos and muon neutrinos are created from muon decay processes. Due to neutrino oscillations, the distribution of the flavours is equal in the observer's frame. The production rate from pion decay for muon neutrinos is given by

$$Q^\pi_{\nu_\mu}(E_{\nu_\mu}) = \frac{1}{m_\mu c^2}\int_{\frac{E_{\nu_\mu}}{m_\pi c^2(1-r_M)}}^{\infty} \frac{d\gamma_\mu}{\gamma_\pi}\frac{Q_{\mu^\pm}(\gamma_\mu)}{1-r_M} \tag{3.14}$$

with $r_M = (m_\mu/m_\pi)^2$.

From muon decay, the production rate of muon neutrinos and electron neutrinos is given by

$$Q^\mu_{\nu_\pm} = \frac{1}{m_\mu c^2}\int_0^1 dy\,\frac{Q^\mu_e(E_{\nu_i}/y)}{y}\frac{dn}{dy} \tag{3.15}$$

where $y = E_{\nu_i}/E_\mu$ and $Q^\mu_e = n'_{\mu^i}(\chi)/(\gamma t'_{\mu^i,decay})$, with primed reference frame being in the laboratory frame. The neutrino production rate in the lab frame is given by

$$\frac{dn}{dy} \approx g_0(y) + g_1(y) \tag{3.16}$$

where g_0 and g_1 are functions summarized in Table 3.1. Neutrino power in the observer's frame is assumed to be equally distributed across the flavours due to neutrino oscillations with the antineutrinos and neutrinos not distinguished.

Evolution of electrons

Primary electrons are injected using Equation 3.4, then lose momentum due to synchrotron, adiabatic and inverse-Compton. Unlike protons, electrons are also created from secondary processes such as BH pair production, $\gamma - \gamma$ pair production and muon decay. Secondary electrons also lose momentum from the processes mentioned above for primary electrons. Electrons are stable particles so the decay term from Equation 3.2 will be 0. Fokker-Planck for electrons is then solved.

3.1.2 Radiative evolution

This section provides a summary of how we handle the radiation terms in OneHaLe. We use the radiative transfer equation (RTE) to compute the photon distribution at equilibrium. The RTE is a differential equation that describes the change of radiance (L) along a ray of light in a medium. The radiance is the energy flow per unit area per unit solid angle per unit time. The RTE can be written as

$$\frac{\partial n_{ph}(v,t)}{\partial t} = \frac{4\pi}{hv} j_v(t) - n_{ph}(v,t) \left(\frac{1}{t_{esc,ph}} + \frac{1}{t_{abs}} \right) \tag{3.17}$$

where j_v is the emissivity for all radiation processes, $t_{esc,ph}$ is the photon escape time-scale from a slice of size Δz, t_{abs} is the absorption time-scale due to synchrotron self-absorption and pair production. The spectral luminosity in the observer's frame is then obtained by

$$v^{obs} L^{obs}_{v^{obs}} = \delta^3 \frac{hv^2 V_{co}}{t_{esc,ph}} n_{ph}(v,t) \tag{3.18}$$

where n_{ph} is the photon number density, V_{co} is the co-moving volume, and δ is the Doppler boost. The absorption time scale is given by

$$t_{abs} = \frac{\Delta z}{c\left(\tau_{SSA}(v) + \tau_{\gamma\gamma}(\epsilon)\right)} \tag{3.19}$$

where τ_{SSA} and $\tau\gamma\gamma$ are the opacities for synchrotron self-absorption and pair production, respectively. We evaluate the emissivity from various radiation processes such as synchrotron, inverse Compton with external photons, neutral pion decay,

inverse-Compton from isotropic photon fields and synchrotron self-Compton using the equations given in [12].

External photons

The AD, the BLR, the DT and the CMB are four sources of external photons that can interact with the jet of a blazar. We assume that the jet is powered by a fraction of the accretion power onto a supermassive black hole, so that $\hat{L}_{AD} = l_{edd} L_{edd}$, where L_{edd} is the Eddington luminosity and l_{edd} is the Eddington ratio. The Eddington luminosity depends on the mass of the black hole M_0, the proton mass m_p, the speed of light c, and the Thomson cross-section σ_T, as $L_{edd} = 4\pi G M_0 m_p c/\sigma_T$. We adopt a thin-disc model for the AD, which extends from the innermost stable orbit to a maximum radius where the disc becomes unstable due to self-gravity. This radius is given by

$$\hat{R}_{AD,max} = 1680 R_g \left(\frac{M_0}{10^9 M_\odot}\right)^{-2/9} \alpha^{2/9} l_{edd}^{4/9} \left(\frac{\xi}{0.1}\right)^{-4/9} \text{cm} \tag{3.20}$$

where α is the disc viscosity parameter, and ξ is the mass-to-radiation conversion efficiency. The temperature of the AD as a function of its radius $\hat{r}_{AD}$ is given by

$$\hat{T}_{AD}(\hat{r}_{AD}) = \left(\frac{3 G M_0 \hat{L}_{AD}}{8\pi\xi c^2 \sigma_T \hat{r}_{AD}^3}\right)^{1/4}. \tag{3.21}$$

A grey body radiator is used to model the BLR and DT, which are imperfect radiators that partially absorb and emit incident electromagnetic radiation. The temperature of the BLR and DT is denoted by $\hat{T}_{BLR}$ and $\hat{T}_{DT}$, respectively. The radius of each radiator is given by the following equations:

$$\hat{R}_{DT} = 2.5 \times 10^{18} \left(\frac{l_{edd} L_{edd}}{10^{45} \text{erg s}^{-1}}\right)^{1/2} \text{cm} \tag{3.22}$$

$$\hat{R}_{BLR} = 10^{17} \left(\frac{l_{edd} L_{edd}}{10^{45} \text{erg s}^{-1}}\right)^{1/2} \text{cm} \tag{3.23}$$

where l_{edd} is the Eddington ratio and L_{edd} is the Eddington luminosity. The luminosity of each radiator in the galaxy frame, assuming isotropy, is calculated as a function of the distance z from the galaxy, as follows:

$$\hat{L}_{BLR} = \frac{0.1 l_{edd} L_{edd}}{(1 + z/\hat{R}_{BLR})^3} \tag{3.24}$$

$$\hat{L}_{DT} = \frac{0.1 l_{edd} L_{edd}}{(1 + z/\hat{R}_{DT})^4} \tag{3.25}$$

OneHaLe is a code that takes some input parameters and outputs the spectral fluxes for all particles and fields in the observer's frame. It also outputs other properties that are not relevant for our purpose, such as light curves. The input parameters for OneHaLe are listed in Table 4.1.

3.2 CALCRATE

CALCRATE is a software tool developed for KM3NeT. It allows users to estimate neutrino and background rates, as well as discovery potential and sensitivity, for different types of neutrino sources. It employs a cut-and-count method, where the rates, discoveries and sensitivities are computed for various combinations of energy and angular cuts. It can handle both point-like and diffuse neutrino sources, and accounts for the background from atmospheric muons and neutrinos, bioluminescence and K^{40}-decay. The signal and background rates are used to evaluate the sensitivity and discovery criteria based on statistical methods.

3.2.1 Rates

In general the neutrino rates are calculated using

$$Rate(E, \theta) = \int\int\int A_{eff}(E', \cos\theta') F(E') D(E', E, \cos\theta) P(E', \cos\theta', \cos\theta) dE' d\Omega' dt \tag{3.26}$$

To predict the neutrino rate in each energy bin, one needs to account for the detection efficiency of the instrument and the selection criteria applied to the data. The instrument response function (IRF) is used to calculate the effective area of detection, $A_{eff}(E', \cos\theta')$, which depends on the energy and direction of the incoming neutrinos. This is multiplied by the neutrino flux, $F(E')$, which is the intensity of neutrinos per unit area and energy. Then, it is multiplied by ΔE, which is the width of each energy bin, and T, which is the duration of the observation of the neutrinos and the angular bin size $I_\theta = 2\pi \cdot [\cos(\theta_{max}) - \cos(\theta_{min})]$, where θ_{max} and θ_{min} are the maximum and minimum angle of generation. Finally, it is multiplied by $D(E', E, \cos\theta)$ and $P(E', \cos\theta', \cos\theta)$, which are correction factors that account for the energy dispersion and point spread function of the detector. The resulting

expression for the neutrino rate is

$$Rate(E,\theta) = T \sum_{E'} \sum_{\cos\theta'} A_{eff}(E', \cos\theta') * F(E') * \Delta E * D(E', E, \cos\theta) * P(E', \cos\theta', \cos\theta) * I_\theta \tag{3.27}$$

Background rate estimates used are from atmospheric muons and neutrinos using Monte Carlo simulations.

Instrument response function

The KM3NeT is not yet fully operational, so Markov-Chain Monte Carlo (MCMC) simulations are used to generate events that mimic the instrument response function. One year of observation time is assumed. Three different sources of neutrinos to are used to simulate the events: atmospheric conventional neutrinos, atmospheric prompt neutrinos and cosmic neutrinos. The atmospheric conventional neutrinos are based on the Honda model [49], which uses a virtual detector to calculate the neutrino fluxes. The atmospheric prompt neutrinos are based on the ERS model [50], which accounts for the charm production in the atmosphere due to cosmic rays. Both models are adjusted for the cosmic-ray spectrum knee used by Gaisser[51]. The cosmic neutrinos are assumed to follow a diffuse flux given by

$$\Phi_{\nu_i+\bar{\nu}_i} = 1.2 \times 10^{-4} E^{-2}_{\nu_i+\bar{\nu}_i} (GeV^{-1} m^{-2} s^{-1} sr^{-1}) \tag{3.28}$$

where E_ν is the neutrino energy. More realistic cosmic neutrino spectra are not yet implemented in CALCRATE (KM3NeT internal document, 2023, *Combined track and cascade selection with ARCA115v9*).

Track reconstruction

To reconstruct an event in a Cherenkov detector that is working properly, the tracks of the particles that produce Cherenkov light are used. The most important track is the one from the muon with the highest energy in the event, which will generate at least one Cherenkov photon that hits two different DOMS. This track is used to select events that are suitable for studying the detector response. The quality of the reconstructed track depends on two criteria:[52]

- The number of DOMS that detect Cherenkov photons from the highest energy muon must be at least two.

- The angle between the direction of the highest energy muon and the reconstructed track must be less than 10°.

To optimize the selection of neutrino events, four kinds of cuts are applied: track, direction, background-like and signal-like cuts. I will explain each of them briefly.

Track cuts: Only events with a reconstructed track that has a positive likelihood, positive length and energies above 10 GeV are accepted by this cut.

Direction cut: This cut selects tracks that are upgoing or horizontal, meaning that they have a reconstructed angle θ_{rec} between 0° and 100°.

Background-like cut: This cut removes tracks that are poorly reconstructed and belong to a region where the signal is negligible.

Signal-like cut: This cut reduces the background contamination by applying a separate criterion for events with a reconstructed neutrino energy $E_{track,rec}$ higher than 10^6 GeV or $E_{track,rec} > 10^6$ GeV. This is the energy above which we expect the cosmic neutrino flux to be higher than the atmospheric neutrino flux. These events are also the most likely to be well reconstructed.

To further reduce the events that are not signal-like but are background-like, a final cut is applied based on a Boosted Decision Tree (BDT). The BDT is a machine learning algorithm that combines multiple weak learners (such as shallow trees) in a sequential way, where each learner tries to correct the error of the previous one. The BDT uses the Gradient boosting method, which adjusts the weights of the learners according to their performance. The BDT score is a measure of how signal-like an event is, and it depends on the direction of the track. For up-going tracks, the BDT score must be greater than 0.4, and for horizontal tracks, it must be greater than 0.9.

Cascade/Shower reconstruction

For cascade channel, the signal is defined as:

- The event must contain a ν_μ particle.

- The interaction vertex must be inside the detector.

- The angle between the reconstructed shower and the most energetic muon must be less than 10°.

Four cuts to the reconstructed showers are applied, namely: reconstruction status, containment, Cherenkov hits and total number of hits. In addition, a BDT is used to select events with short showers. Here is a brief explanation of each cut,

Reconstruction status: Only select events that have both a track and a shower reconstruction. The cascade selection uses information from both reconstruction algorithms and we note that no signal events are lost by also selecting for a completed track reconstruction.

Containment: Only events that have a vertex far from the edge of the detector and have a reconstructed vertex $R > 500$ m are selected. Events are required that the height $Z < 650$ m.

Cherenkov hits: These are hits that are produced by Cherenkov radiation near a detector. The hits that has at least $N_{Cherenkov} > 10$ are selected, to ensure that the event is consistent with a cascade hypothesis.

Total number of hits: Each event must have a minimum number of hits given by $\log_{10}(N_{hits}) > 2.6$.

For events with short showers ($l < 300$ m), a BDT cut is applied based on the reconstructed shower energy. The BDT cascade score must satisfy

$$\text{BDT cascade score} > -0.7 \log_{10}(E_{shower,rec}) + 2.9 \tag{3.29}$$

The events which are selected after the cuts using a likelihood test are then used to calculate $A_{eff}(E, \cos\theta)$, $D(E', E, \cos\theta)$ and $P(E, \cos\theta', \cos\theta)$. These are also known as instrument response functions (IRFs).

3.2.2 Discovery and Sensitivity

In a counting experiment, the main aim is right in the name which is to count the number of events detected by a detector during the observation period. In neutrino counting experiments atmospheric neutrinos are the most abundant, and a detected event usually has a source and background signal. However, we are interested in

counting the number of cosmic neutrino events, thus, atmospheric neutrinos will be part of the background events. Event detection is claimed if it can be proven that the event is significantly different from the background, hence reducing what is called chance detection. If an event cannot be significantly distinguished from the background, the best detection setting is established.

We define a discovery as the rejection of the background-only hypothesis with a high level of confidence. Subsequently, sensitivity is defined as the average upper limit on the source flux in which detection can be claimed. In this section, we will be discussing how the source discovery and sensitivity were calculated.

Discovery

Discovery potential is found using the total number of detected events, n_α, with a probability α or less to originate from a pure background source in $(1-\beta)\%$ of all hypothetical experiments[1]. Suppose we want to make a 5σ detection, then the chance probability is $\alpha \approx 3 \times 10^{-7}$ or 1 in 3.5 million that the detection occurred by chance. To calculate n_α, we find the least detectable signal mean μ or n_0 which is the number of observed events needed to deviate from the background-only hypothesis at the given α, and this is given by

$$\sum_{n_{obs} \equiv n_0}^{\infty} P(n_{obs}|n_b) \leq \alpha \tag{3.30}$$

where $n_{obs} = n_s + n_b$ with n_s being the signal mean and background mean n_b. The critical number of observed events to deviate from the background is given by n_α. The probability of deviating from the background in $(1-\beta)\%$ of hypothetical experiment by 5σ is given by

$$P_{5\sigma} = \sum_{n_{obs} \equiv n_0}^{\infty} P(n_{obs}|n_b + n_\alpha) = 1 - \beta \tag{3.31}$$

thus, the minimum flux needed for discovery is

$$\Phi_\alpha(E, \theta) = \Phi(E, \theta) \frac{n_\alpha(n_b)}{n_s}, \tag{3.32}$$

where $\frac{n_\alpha}{n_s}$ is the model detection potential (MDP).[53]

[1] β is the discovery power and $1-\beta$ is the statistical power

Sensitivity

Suppose the source is not significantly detected, an average upper limit is imposed on the flux and it is found using the 90% confidence level. Using the Feldman-Cousins method[54], the 90% confidence level for the signal mean is given by

$$\bar{\mu}_{90}(n_b) = \sum_{n_{obs}=0}^{\infty} \mu_{90}(n_{obs}, n_b) \frac{(n_b)^{n_{obs}}}{n_{obs}!} \exp(-n_b) \tag{3.33}$$

$\mu_{90}(n_{obs}, n_b)$ is calculated assuming that there is no source detected ($n_s = 0$).

Determination of $\mu_{90}(n_{obs}, n_b)$

Assuming the event counting with a known background rate b is given by

$$P(X = n|\mu) = \mathcal{L}(\mu|X) = (\mu + b)^n \frac{e^{-(\mu+b)}}{n!} \tag{3.34}$$

where μ is the signal mean rate. Confidence level (α) is defined as the probability that an estimator of a population parameter has the same location as the estimated parameter. For instance, if a confidence interval was calculated at 95% confidence level for a given sample, then there is a 95% chance that the population mean rate parameter lies within the calculated interval. Therefore, the probability for a subset member[2] of μ, represented by x, in the confidence interval $[x_1, x_2]$ to be an estimator ($\hat{\mu}$) of a population mean rate, μ, is α. This can be written as

$$P(x \in [x_1, x_2]|\mu) \geq \alpha, \tag{3.35}$$

with the "$\geq$" used for avoiding under-coverage of events. For an event counting experiment with a required 90% confidence level, Equation 3.35 becomes

$$P(n \in [n_1, n_2]|\mu) \geq 0.9 \tag{3.36}$$

with the sample now being the number of detected events. Using Equation 3.34 and Equation 3.36 we can solve for $\mu_{90}(n_{obs}, n_b)$.

Equation 3.33 is for a single experiment, however, to impose an average upper limit on the flux an average $\bar{\mu}(n_b)$ is needed and it can be found by using a statistical ensemble. The result of the ensemble is denoted by just $\bar{n}_{90}$. Hence, the upper limit

[2]This is also called a "sample"

flux is given by

$$\bar{\Phi}_{90}(E,\theta) = \Phi(E,\theta)\frac{\bar{n}_{90}}{n_s} \tag{3.37}$$

where $\frac{\bar{n}_{90}}{n_s}$ is called the model rejection factor (MRF).

Chapter 4

Methodology

We will now show how the results in this project were obtained. We used OneHaLe to estimated the neutrino fluxes by first fitting the simulated blazar with archival data for 3C 279. We used the neutrino fluxes to then estimate the KM3NeT neutrino detection potential and sensitivity. We then compared the upper limit flux with those of existing telescopes such as IceCube.

4.1 SED

We present the results of our spectral energy distribution (SED) obtained from simulating a blazar jet with OneHaLe, a code that calculates the fluxes, light-curves and other distributions of photons, electrons and protons in a jet. We focus on the neutrino emission from different processes involving these particles. We use the parameters listed in Table 4.1 for our simulation.

OneHaLe requires two types of input parameters: those that depend on the source and those that do not. The source-dependent parameters are obtained from observations of the specific source, such as z, M, l_{edd}, $\hat{R}_{BLR}$, $\hat{T}_{BLR}$, $\hat{L}_{BLR}$, $\hat{R}_{DT}$, $\hat{T}_{DT}$ and $\hat{L}_{BLR}$. For 3C 279, which we use as an example, we adopt similar values for these parameters as in [25].

The source-independent parameters are determined by the physical processes that occur in the blazar jets. The magnetic field is one of the most important free parameters, but we assume it is constant. We show the results in Figure 5.1 and perform a qualitative fit due to the high number of free parameters (about 36 in

Value	Symbol	Description	Units
120	B	Magnetic field of the homogeneous region	G
8.65×10^{16}	R	Blob radius	cm
20	η_{esc}	Ratio of the acceleration to escape time scales	
0.536	z	Redshift to the source	
25	Γ	Bulk Lorentz factor for the blob	
5.67×10^{-2}	θ^{obs}	Observing angle relative to the axis of the BH jet	rad
1.01	$\gamma_{min,p}$	Minimum Lorentz factor for the proton injection spectrum	
2.00×10^{9}	$\gamma_{max,p}$	Maximum Lorentz factor for the proton injection spectrum	
1.60	q_p	Proton injection index	
1.0×10^{44}	$L_{inj,p}$	Injection luminosity for the proton spectrum	$\mathrm{erg\,s^{-1}}$
5.01	$\gamma_{min,e}$	Minimum Lorentz factor for the electron injection spectrum	
2.01×10^{5}	$\gamma_{max,e}$	Maximum Lorentz factor for the electron injection spectrum	
2.40	q_e	Electron spectral index	
1.10×10^{42}	$L_{inj,e}$	Injection luminosity for the electron spectrum	$\mathrm{erg\,s^{-1}}$
20	$\eta R/c$	Multiplicative factor of the light travel time	s
6.0	M	Mass of the supermassive black hole	$1.0 \times 10^{8} M_{\odot}$
1.18×10^{-2}	l_{edd}	Eddington ratio	
7.70×10^{17}	R_0	Initial location of the blob along jet axis	cm
7.61×10^{16}	$\hat{R}_{BLR}$	Radius of the BLR	cm
5.0×10^{3}	$\hat{T}_{BLR}$	Effective temperature of the BLR	K
2.30×10^{44}	$\hat{L}_{BLR}$	Effective luminosity of the BLR	ergs
5.23×10^{18}	$\hat{R}_{DT}$	Radius of the DT	cm
1.5×10^{3}	$\hat{T}_{DT}$	Effective temperature of the DT	K
9.0×10^{44}	$\hat{L}_{DT}$	Effective luminosity of the DT	ergs

Table 4.1: List of OneHaLe free parameters with units

total) and the computational challenges of modelling them.

To find the neutrino fluxes, we used OneHaLe. We used OneHaLe because it is a purely theoretical model which also allows us to estimate the neutrino fluxes. Another reason why we used a lepto-hadronic model was to set up a parameter space study in the modelling of blazars and AGNs in general. However, the use of 3C 279 as an illustrative source was partly based on the lack of neutrinos from blazars in quiescent state and also due to the intensive study of 3C 279 in literature. OneHaLe takes in an input file with free parameters that are used to find the geometry of the blazar jet and the jet material including interactions.

We ran a simulation with the parameters listed in Table 4.1. When the simulation was complete, fluxes in observer's frame were found in the output and plotted. A fit-by-eye technique was used to fit to plot due to the level of computational complexity and power one would need to fit all free parameters from OneHaLe.

To perform the fit-by-eye, we started with the base parameters used by M. Zacharais in [25]. The initial parameters did not fit the archival data, so we had to change the

parameters, which were not source dependent such as the magnetic field, injection luminosities, spectral indexes and Lorentz factors (both maximum and minimum). We changed the parameters, one at a time, to ensure that we understood the sensitivity of the fit to changes in the parameters. However, as seen in Table 4.1, the magnetic field and the proton injection spectrum produced by this manually perturbative process were incorrect.

An early fit using the magnetic field of 0.25 G, shown in Figure 4.1, could not fit the data. A similar study by C. Diltz[9] using the previous version of OneHaLe, suggested that a magnetic field of around 150 G was needed to fit 3C 279, also using a "fit-by-eye" technique. This prompted the increase of the magnetic field from 0.25 G to 150 G. After several iterations of the magnetic field to fit better the high energy data, a magnetic field of 120 G and proton injection index of 1.60 provided us with a fit which was deemed to be a bit sufficient.

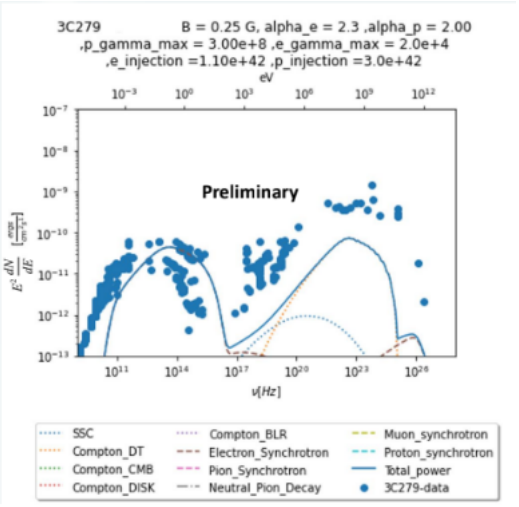

Figure 4.1: An early fit of the 3C 279 SED using the 'fit-by-eye' method ' to 3C 279 archival data found on NED.

The parameters which depend on observations of relativistic effects in the jet such as the bulk Lorentz factor, acceleration to escape timescales and multiplicative factors of light travel time were allowed to match that of [12].

OneHaLe outputs the simulated SED, as well as neutrino fluxes, so once an approximate fit was done the neutrino fluxes were assumed to be correct.

4.2 CALCRATE methods

This section presents the simulated detection rates, discovery potential and sensitivity for ν_μ and ν_e events. We use CALCRATE to perform these calculations, which requires several input parameters. These parameters can be divided into two (2) categories, but we will enumerate them all. Table 4.2 shows the list of parameters used in our analysis. In this section, we will briefly review the different input options

Option	Description
f	RDF/ingredients ROOT files
m	output-type
F	neutrino flux expression [1/(GeV m2 s sr)]
g	flux expression refers to gamma-rays
T	livetime (s)
YR	years of observation
t	Neutrino flavour interactions
c	observational channels
p	point source mode (flux in /GeVm2s)
d	declination(range) for point-mode (degrees)
a	search cone radius(range) for point-mode (degrees)
e	minimal log of reconstructed energy (range)
w	source width (degrees)
u	source shape (if width > 0); 0=disk, 1=gaus
z	confidence level for limits
s	significance level for discovery
b	1-b statistical power for discovery

Table 4.2: Table showing the list of input options used for CALCRATE

for our analysis, with an emphasis on those that are not based on statistical methods. The option "f" specifies the detector file that contains the information needed to compute the IRFs, which are used by CALCRATE to calculate the background and signal rates. Options "F" and "g" are related to the neutrino fluxes, where "F" is the neutrino flux given in the units shown on Table 4.2 and "g" uses the gamma-ray flux to infer the neutrino flux. The options "t" and "c" account for the neutrino interactions and observation channels, respectively. The channels are track and shower, which correspond to different types of events produced by neutrinos in the detector.

4.2.1 Rates, sensitivity and discovery

The output file for neutrino fluxes were used to produce the rates, sensitivity and discovery. We exported the file into the KM3NeT servers, and used CALCRATE with following input parameters (refer to Table 4.2 for full description):

- m - mrf, opt, rates
- t - shower, track
- T - 1 year

- c - numuCC, nueCC
- a - 0:5:1
- e - 1:8:1
- w - 0
- u - not needed
- z - 0.9
- s - 5sigma
- b - 0.2
- d - declination (°)

Options a and e can be summarized as start:end:step. To find the right ranges for "e", we calculated the neutrino rates across all the energy cuts to determine the energies where the detector response is zero. Using this, we were able to find the lower and upper energy cuts. For "a", the input parameters were set to the newly obtained limits for "e", meaning that "e" would be 1:8:1, and we searched for the maximum cone search angle that would optimize the MRF for shower events. To do this, the cone search angle was set to be 0:90:0 and the optimal MRF was found. The optimal MRF was found to be located near 5°; we then set the range for the viewing angle using the above angle.

To find the initial results, the declination was set at the declination of the source (3C 279). We found the optimized MRF and MDP within the ranges of energy cuts and cone viewing angles. For individual particle detections, option "t" was set to just "numuCC" or "nueCC" in the appropriate channel "c" of "track" or "shower". The input for combined signals was set as "t - numuCC, nueCC". In the case of combined shower events, the cone viewing angle and minimum energy cuts at the optimized MRF and MDP were inconsistent with what was expected. Hence, we produced an MRF table to find the bin the where the optimal MRF and MDP are likely to be located.

To find the results in all declinations, the declination was set at $-90° < \delta < 90°$.

Then we repeated the procedure in the first part to find the optimized MDP and MRF. We then compared the uppper flux limit for the most sensitive flux with that from literature.

Chapter 5

Results

5.1 Results of OneHaLe

Due to the quantum mechanical phenomenon of neutrino oscillation, which implies that neutrinos have non-zero mass and can change their lepton flavor as they propagate through space, the neutrino fluxes observed at Earth are equal for ν_e, ν_μ and ν_τ. The neutrino spectrum shown in Figure 5.2 is based on an estimated SED, which is not exact. This means that the neutrino spectrum in Figure 5.2 is also approximated.

Figure 5.1 illustrates a simulated blazar jet SED which is dominated by proton emission at higher energies. However, the SED does not completely fit the NED archival data of 3C 279 due to a few reasons. One possible reason is that the use of a fit-by-eye technique does not allow us to find the best-fit of the model to data. Another possible reason is that the SED does not account for the variability and orientation effects as the blazar jet evolves, which can affect the observed radiation across different wavelengths.

Neutrinos in the observer's frame (see Figure 5.2) have a spectrum that cannot be modelled by an analytic function, meaning that the input spectrum for CALCRATE is provided as a table of differential fluxes as a function of energy rather than an analytic function. The differences between the neutrino spectra found in the literature[31] and our simulated fluxes could be due to the hard spectrum of the injected protons with $\alpha = 1.6$ and $\gamma_{max} = 2 \times 10^9$ used. There is a possibility that all protons undergo proton synchrotron radiation due to the high magnetic fields.

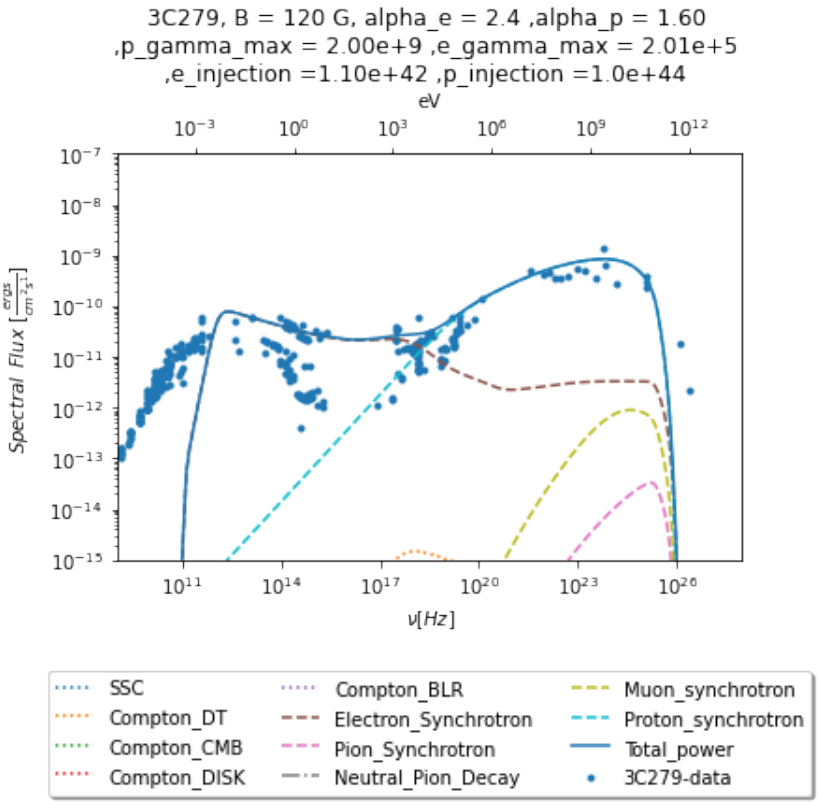

Figure 5.1: SED 'fitted-by-eye' to 3C 279 archival data found on NED. Solid line represents the total neutrino flux, and the dotted lines represent neutrinos produced from the different neutrino processes. Some of the input parameters are displayed.

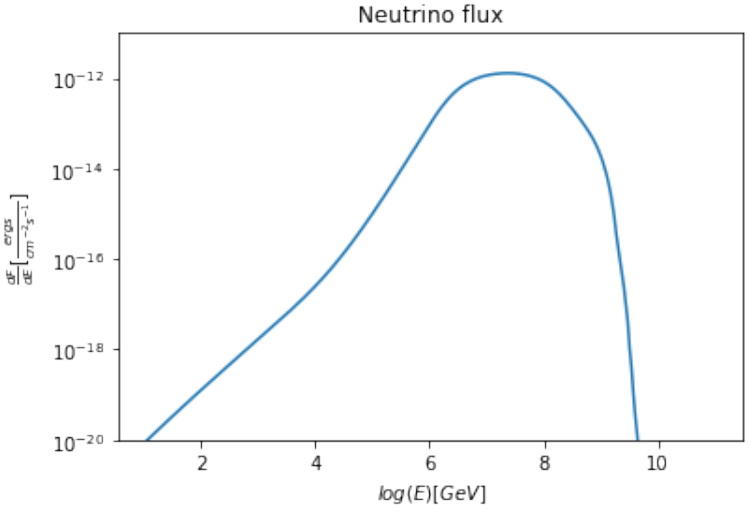

Figure 5.2: Neutrino fluxes corresponding to the SED in Figure 5.1.

5.2 Results of CALCRATE

5.2.1 Neutrino Sensitivity, Discovery and Rates

We aimed to identify the optimal neutrino fluxes that can be detected, excluding the ν_τ flavour. For this purpose, we needed to know the best detector configuration, which we defined as the optimal directional and energy cuts. We used CALCRATE to simulate the sample source 3C 279, which has a declination of $-05°47'22''$, and we calculated the optimal configuration for different neutrino flavours and neutrino interaction channels that would achieve a 5σ discovery, chance probability of 3×10^{-7}, with a statistical power for discovery of 0.2. We used 3C 279 as an illustrative source, however, the discovery power is derived from the elusive nature of neutrinos, and factoring in the possibility that astrophysical neutrinos sources may be dominated by sources which may not necessarily be blazars or even AGNs. Since, the study is also for all blazar sources, not necessarily 3C 279, we chose the 5σ discovery as most of the blazar neutrino source are not well known so we want the source signal to be as different as possible from the background. We used the optimized MRF and MDP methods, and we assumed 1 year of observation time. The results are shown below: We observed that shower events have larger cone viewing angles

decl(rad)	cone(opt)	minlogE(opt)	total-sig	total_bg	mean limit	MRF	n limit discovery	MDP
-0.101043	0.363078	4.49694	0.0130742	0.00107118	2.30321	176.165	0.9	68.8378

Table 5.1: The optimized simulated discoveries and sensitivities for a ν_μ detected using the track channel.

decl(rad)	cone(opt)	minlogE(opt)	total-sig	total_bg	mean limit	MRF	n limit discovery	MDP
-0.101043	1.99699	0.585471	1.58903e-06	0.00624475	2.30625	1.45135e+06	1.6	1.0069e+06

Table 5.2: The optimized simulated discoveries and sensitivities for a ν_e detected using the track channel.

decl(rad)	cone(opt)	minlogE(opt)	total-sig	total_bg	mean limit	MRF	n limit discovery	MDP
-0.101043	1.99538	4.42582	0.000669623	0.413577	2.30321	3439.57	0.9	1344.04

Table 5.3: The optimized simulated discoveries and sensitivities for a ν_e detected using the shower channel.

decl(rad)	cone(opt)	minlogE(opt)	total-sig	total_bg	mean limit	MRF	n limit discovery	MDP
-0.101043	1.99526	4.50134	0.000120985	0.382902	2.30321	19037.2	0.9	7438.94

Table 5.4: The optimized simulated discoveries and sensitivities for a ν_μ using the shower channel.

(in degrees) than track events, as expected. We also noticed that muon neutrinos

(ν_μ) are more likely to be detected than other neutrino flavours, because they have the lowest values of MDP and MRF. On the other hand, electron neutrinos (ν_e) and muon neutrinos from track and shower interactions, respectively, are less likely to be detected. This implies that track-like events are mainly caused by muon neutrinos, while shower-like events are mainly caused by electron neutrinos. However, both neutrino flavours can contribute to both types of events.

We assumed that the background is uniform and that the events are independent of each other. Based on these assumptions, we calculated the detector limits or configurations using the tables above. However, these assumptions are not very realistic, so we decided to refine our analysis. We considered that both muon and electron neutrinos can be detected in both shower and track events (we used model fitting to distinguish between them), so we included both neutrino flavours in each interaction channel. The results are shown below.

decl(rad)	cone(opt)	minlogE(opt)	total-sig	total_bg	mean limit	MRF	n limit discovery	MDP
-0.101043	0.363078	4.49728	0.013073	0.00107118	2.30321	176.181	0.9	68.8443

Table 5.5: The optimized simulated discoveries and sensitivities for combined ν_μ, ν_e using the track channel.

decl(rad)	cone(opt)	minlogE(opt)	total-sig	total_bg	mean limit	MRF	n limit discovery	MDP
-0.101043	1.99966	0.0928499	0.000817171	0.382902	2.51678	3079.87	4.4	5384.43

Table 5.6: The optimized simulated discoveries and sensitivities for combined ν_μ, ν_e using the shower channel.

We observe a slight reduction in the total signal of both electron and muon neutrino events, which leads to a slight reduction in the MDP and MRF. The reason for this reduction is the higher background events due to the detector being sensitive to both types of neutrinos. This also avoids the potential problems that could arise from separating neutrino events such as significantly underestimating the signal or missing about two thirds (2/3) of the flux from the same source. When we compare Table 5.3 and Table 5.6, we see that in the latter, the optimal viewing angle size matches that of a shower event from a point source, but the optimal effective energy is even lower than that of individual neutrino species. When we compare the MRF table for shower events and the optimal MRF table for the combined signal ν_μ, ν_e, we see that the result is not as optimal as expected. The bin where we would expect to find the optimal MDP and MRF is shown in Figure 5.3.

We have performed simulations of neutrino fluxes from 3C 279. Our results, shown in

cone	minloge	total-sig	total-bg	meanlimit	MRF	n limit discovery	MDP
1	1	0.000298503	0.0957651	2.35812	7899.79	3	10050.1
1	2	0.000298503	0.0957651	2.35812	7899.79	3	10050.1
1	3	0.000298416	0.0706783	2.3437	7853.81	3.1	10388.2
1	4	0.000295213	0.00407538	2.30498	7807.83	1.6	5419.81
1	5	0.000279762	5.05159e-05	2.30261	8230.61	0.9	3217.02
1	6	0.000227152	3.09233e-07	2.30259	10136.7	0.3	1320.7
1	7	4.79665e-05	9.68961e-10	2.30259	48004	0.3	6254.36
2	1	0.000817171	0.383031	2.51685	3079.95	4.4	5384.43
2	2	0.000817171	0.383031	2.51685	3079.95	4.4	5384.43
2	3	0.000816928	0.282692	2.46268	3014.56	3.7	4529.16
2	4	0.000807518	0.0163003	2.31214	2863.26	2.3	2848.23
2	5	0.000762444	0.000202048	2.3027	3020.16	0.9	1180.41
2	6	0.000616306	1.23684e-06	2.30259	3736.11	0.9	1460.31
2	7	0.000139685	3.87555e-09	2.30259	16484.1	0.3	2147.69
3	1	0.00122227	0.861711	2.75867	2257	5.6	4581.63
3	2	0.00122227	0.861711	2.75867	2257	5.6	4581.63
3	3	0.00122189	0.635976	2.64786	2167.02	5	4092.02
3	4	0.00120688	0.036671	2.32401	1925.63	2.3	1905.73
3	5	0.00113586	0.00045455	2.30285	2027.4	0.9	792.348
3	6	0.000918214	2.78253e-06	2.30259	2507.68	0.9	980.163
3	7	0.000217955	8.71888e-09	2.30259	10564.5	0.3	1376.43
4	1	0.00151017	1.53166	3.05904	2025.62	7.5	4966.32
4	2	0.00151017	1.53166	3.05904	2025.62	7.5	4966.32
4	3	0.00150966	1.13042	2.88388	1910.29	6.2	4106.89
4	4	0.00148985	0.0651813	2.34053	1570.98	3.1	2080.74
4	5	0.00139644	0.000807946	2.30306	1649.24	0.9	644.497
4	6	0.0011274	4.94585e-06	2.30259	2042.39	0.9	798.298
4	7	0.000278844	1.54975e-08	2.30259	8257.61	0.3	1075.87
5	1	0.00167573	2.39267	3.39628	2026.75	8.5	5072.42
5	2	0.00167573	2.39267	3.39628	2026.75	8.5	5072.42
5	3	0.00167512	1.76588	3.15555	1883.77	7.3	4357.89
5	4	0.00165199	0.101823	2.36158	1429.54	3	1815.99
5	5	0.00154311	0.00126213	2.30333	1492.65	1.6	1036.86
5	6	0.00124259	7.72612e-06	2.30259	1853.06	0.9	724.293
5	7	0.000315619	2.42093e-08	2.30259	7295.46	0.3	950.514

Table 5.7: Simulated discoveries and sensitivities for combined ν_μ, ν_e through the shower channel.

Figure 5.2, indicate that the detection of neutrinos from this source is unlikely given our choice of parameters since MRF and MDP are above 1 for all tested energies. To explore the possibility of detecting neutrinos with similar fluxes from other sources, we have scanned the across all declinations for optimal MRF and MDP values for combined shower and track signals. The results of this scan are presented in Figure 5.4.

As shown in Figure 5.5, our signals were dominated by background noise. The source signal was weaker than the background for all optimized MRF and MDP in all declinations. This suggests that the source was either too dim or too distant. The

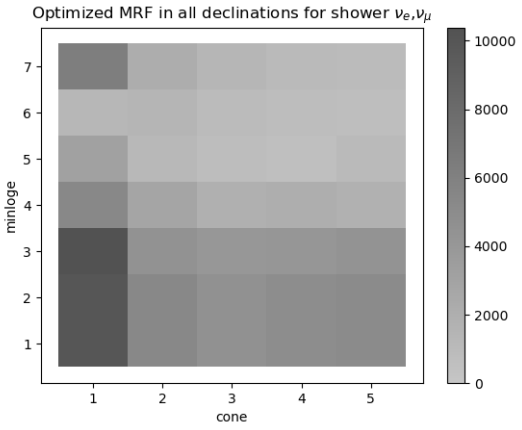

Figure 5.3: Histogram showing MDP binned by effective energy and the viewing angle. The bin centred at (4,5) has the optimized MDP and MRF, the MDP is 644.50 and the MRF is 1649.24.

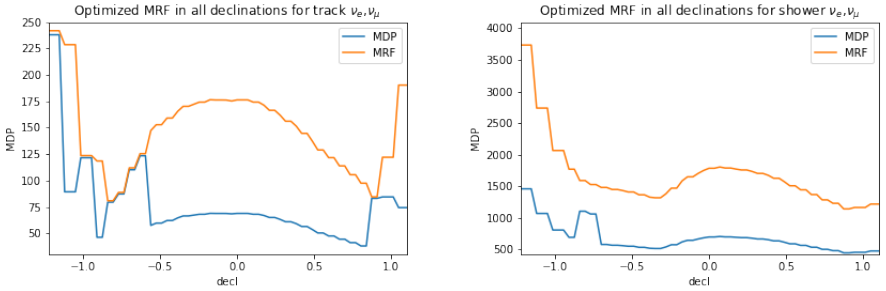

Figure 5.4: MRF and MDP for combined signal detected through the track and shower channel. Effective energy and the cone viewing angle are set to be at 1° and $\log E = 5$ for track events. In shower events, the effective energy and the cone viewing are set to be at 4° and $\log E = 5$

background shown in these figures is the detector specific background, hence showing the performance of the detector at different declinations. It shows that at extreme declinations, the detector may have lower performance. Another reason could be that the event reconstruction algorithm used does not perform that well around $-90°$ and 90°. We explore the potential causes of this result and its implications for future research in Conclusion.

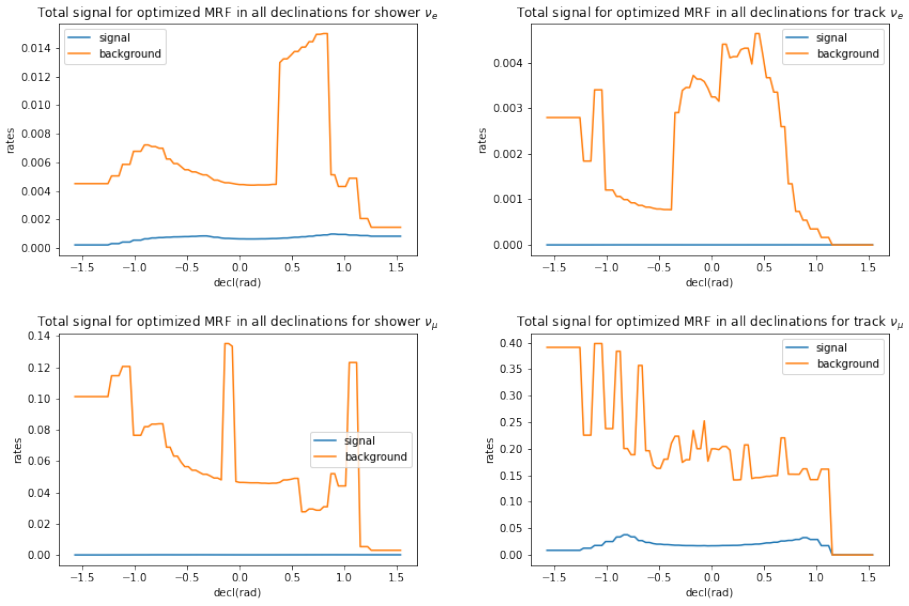

Figure 5.5: Signal and background rates, for the optimized MRF and MDP for both shower and track events. Blue line is for the signal rates and the orange line is for background rates. The above plots illustrate that the source is background-dominated in all observable directions. Apparent fluctuations in the background signal are due to changes in the optimum energy threshold rather than intrinsic changes in the background or instrument sensitivity.

Chapter 6

Conclusion

6.1 Summary of results

A brief discussion of OneHaLe parameters

OneHaLe requires a redshift for the source, so we chose 3C 279 as an example because it has a known redshift of 0.536 and it has been extensively studied in different wavelengths. We used archival data from various telescopes and instruments to fit the SED of 3C 279 in its non-flaring state, assuming that the emission is dominated by synchrotron radiation from relativistic electrons and protons and their interactions with photons and magnetic fields.

We obtained a reasonable fit to the data with OneHaLe, but we also encountered some challenges and limitations. One of them was the choice of the magnetic field strength (B) and the initial location of the blob (R_0). We found that a high value of B (120 G) and a large value of R_0 (7.7×10^{17} cm) were needed to reproduce the observed SED. However, these values are difficult to justify physically, as they imply a very powerful central engine and a very distant acceleration site for the particles. Moreover, they are incompatible with shock acceleration mechanisms, which are commonly invoked to explain the particle spectra in blazar jets. Another challenge was the choice of the spectral indices for the electrons (p_e) and protons (p_p), which determine the shape of the injected particle distributions. We used values of $q_e = 1.60$ and $q_p = 2.40$, where the proton index is inconsistent with previous studies of 3C 279, due to reasons previously discussed in the above chapters, and those of other blazars. These values imply that the jet is dominated by non-thermal particles.

6.1.1 Some neutrino fluxes at the end of the tunnel

Rather than fit the shape of the neutrino spectrum to an analytical expression, we used the directly tabulated numerical values as input to CALCRATE to calculate the minimum flux to which KM3NeT/ARCA is sensitive as a function of direction.

Flavour + channel	**MDP**	**cone search**	**minlogE_opt**	**Upper Flux Limit (ergs/cm^2/s)**
track ν_μ	68.8378	0.363078	4.49694	1.20719 $\times 10^{-10}$
shower ν_e	1344.04	1.99538	4.42582	2.35701 $\times 10^{-9}$
track ν_μ, ν_e	38.078	0.363078	4.49728	6.67765 $\times 10^{-11}$
shower ν_μ, ν_e	644.50	4.0000	5.00000	1.13024 $\times 10^{-9}$

Table 6.1: Calculated upper flux limits and minimum flux needed for a discovery in each channel. The results were calculated using Equation 3.37, where $\Phi(E, \theta) = 1.75368 \times 10^{-12}$ ergs/cm^2/s for energies 10 GeV to 10^8 GeV.

The results of this project are summarized in Table 6.1, which shows the expected fluxes of neutrinos from different types of point sources that can be detected by KM3NeT/ARCA in one year of observation. The upper flux limit for each channel and neutrino flavour will be optimal at different declinations, as shown in Figure 5.4. The first two rows are for 3C 279, and the last two rows are for any source having the same flux as the one in Figure 5.2 in all sky directions. The most likely to be detected neutrinos are track ν_μ. The minimum flux needed for a 5σ discovery is given by the sensitivity, because for all optimized neutrino interactions and channels the MDP is lower than the MRF. This could be due to the low discovery power of 20%.

The main goal of this project was to determine if KM3NeT telescopes would be able to detect neutrinos from blazars in quiescent state, but this was not fully achieved due to some limitations and choices. Firstly, we decided not to scale the simulated observational time to get fluxes for more than a one year of observations, reasoning that discovery of a background-dominated source would not significantly improve with longer exposure. Secondly, we were limited by the archival data used to estimate the fluxes did not include lightcurves to verify if the sources were in a flaring state or not. These factors could affect the accuracy and reliability of the flux estimates.

However, this project was still valuable as it provided a first estimate of the sensitivity of KM3NeT/ARCA to neutrino point sources using the OneHaLe model. This could help to optimize the search strategies and selection criteria for future observations. Moreover, this project also demonstrated the feasibility of a specialized study of sources using OneHaLe and estimating the neutrino fluxes. This is also not surprising as ANTARES also produced an upper flux limit, for BL Lacs in quiescent

state, as $E^2 d\phi_{\nu_\mu}/dE_\nu \approx 4 - 10 \times 10^{-8}$ GeV cm^{-2}s^{-1} for track [27] and our findings for similar interaction channel and neutrino type is $E^2 d\phi_{\nu_\mu}/dE_\nu \approx 4.16786 \times 10^{-8}$ GeV cm^{-2}s^{-1}.

6.2 Main findings

In summary, it is found that:

- Simulated events are very useful, running a simulation before the actual experiment can help with the expected data. By simulating the neutrino flux from a blazar source and the detector response of KM3NeT, we can estimate the sensitivity and discovery potential of the observatory for different scenarios and assumptions.

- Blazar jet models still rely heavily on getting the model to fit the data, this is why there is a degeneracy when it comes to purely leptonic and purely hadronic models. Both models can explain the observed SEDs with different combinations of parameters, but they have different implications for the neutrino production and detection.

- All the simulations for KM3NeT were run at 5σ discovery and 20% statistical power for discovery. This is an indication that the KM3NeT observatory has great potential to detect neutrino signals from quiescent blazars, if they do exist, considering that we used the final expected configuration of the KM3NeT for 1 year and still got some promising results, as it has been shown that it has better sensitivity for non-flaring blazars than IceCube in its current configuration.

- If we extend the observation time, we may increase the chances of detection and discovery. Moreover, if we combine KM3NeT data with other neutrino observatories, such as IceCube, we may improve the sensitivity and angular resolution of the neutrino sources.

- Archival data from NED is multi-wavelength, however, not ideal to use when modelling blazars because the data is not timestamped and may introduced some inconsistencies in the models.

6.3 Future work

Since we used a 'fit-by-eye' approach, the first thing to do for future study would be studying known candidate neutrino sources. This would greatly improve accuracy of the parameters used. One challenge would be the computational requirement to fit more than 26 free parameters that is used by OneHaLe, so we will use models similar to OneHaLe in order to get the to model those sources. One such neutrino candidate would be TXS0506+056 studied in both flaring and non-flaring state, because it has neutrino fluxes for flaring state. A comparison of the two sets of parameters could be used to help in constraining some of the OneHaLe parameters such the proton index.

OneHaLe is a powerful model that can fit the observed spectra of some blazars and predict their neutrino fluxes. However, it also has some limitations and uncertainties, such as the dependence on several free parameters that are not well constrained by observations. To test and improve OneHaLe, more observational data and theoretical developments are needed. Radio analysis of blazars and AGNs in general could assist in constraining the model and also lead to new insight about these highly energetic objects. These radio observations could be used to find the location of collimation of blazar jets which can be used to introduce a lower limit as to where the emission region is located from the central SMBH. Knowing the such limits could allow us to put a limit on the size of the emission region. In turn, the correct or approximate values could be used for the R and R_0 parameters used in OneHaLe.

Applying OneHaLe model to not just blazars but all the AGNs which have jets, would further assist in constraining OneHaLe and reducing the free parameters too. This type of application could be used to estimate the size of the jet if it was to be applied to fit Radio Galaxies.

For sources with sufficiently high real event rates, data from KM3NeT and IceCube could be combined to improve the total sensitivity. KM3NeT and IceCube could complement each other very well since they are located in opposite hemispheres, hence covering the whole sky with little to no blind spots. For example, down-going events for IceCube would be up-going events for KM3NeT, allowing the background rejection and directional and angular reconstruction of neutrino interactions to be improved.

Other extragalactic sources besides AGNs that are worth studying include Gamma-

Ray Bursts, Supernovae and Tidal Disruption Events, all of which may produce detectable neutrino signals. By combining multi-messenger observations of these sources with theoretical models, we can hope to unravel the mystery of the origin of the highest energy cosmic rays.

References

[1] D. Bose, V. Chitnis, P. Majumdar, and A. Shukla, "Galactic and extragalactic sources of very high energy gamma rays," *The European Physical Journal Special Topics*, vol. 231, no. 1, pp. 27–66, 2022.

[2] R. Simoni, *Studies of supernovae and their remnants based on gamma-ray observations with HESS*. PhD thesis, 2022.

[3] A. Abeysekara, W. Benbow, A. Brill, J. Buckley, J. Christiansen, A. Chromey, M. Daniel, J. Davis, A. Falcone, Q. Feng, *et al.*, "Demonstration of stellar intensity interferometry with the four VERITAS telescopes," *Nature Astronomy*, vol. 4, no. 12, pp. 1164–1169, 2020.

[4] M. Spurio, "Gamma-rays, neutrinos and particle astronomy as messengers of the universe," *Acta Polytechnica CTU Proceedings*, vol. 1, p. 13–19, Dec. 2014.

[5] T. K. Collaboration, "The Control Unit of KM3NeT detectors," *Proceedings of Science*, vol. 358 - International Cosmic Rays Conference, July 2019.

[6] A. Trovato, *Development of reconstruction algorithms for large volume neutrino telescopes and their application to the KM3NeT detector*. PhD thesis, 2014.

[7] I. Collaboration, "Neutrino emission from the direction of the blazar TXS 0506+056 prior to the IceCube-170922A alert," *Science*, vol. 361, pp. 147–151, July 2018.

[8] M. Riordan, "Pauli's ghost: The conception and discovery of neutrinos," *Current Aspects of Neutrino Physics*, p. 1–16, 2001.

[9] C. Diltz, M. Boettcher, and G. Fossati, "Time Dependent Hadronic Modeling of Flat Spectrum Radio Quasars," *The Astrophysical Journal*, vol. 802, p. 133, February 2015.

[10] T. K. Collaboration, "Detection Potential of the KM3NeT Detector for High-Energy Neutrinos from the Fermi Bubbles," *Journal of Astroparticle Physics*, vol. 42, pp. 7–14, February 2013.

[11] M. Boettcher, D. E. Harris, and H. Krawczynski, eds., *Relativistic Jets from Active Galactic Nuclei*, vol. 1. Wiley-VCH Verlag GmbH and Co. KGaA, 1 ed., 2012.

[12] M. Zacharias, A. Reimer, C. Boisson, and A. Zech, "Exhale-jet: An extended hadro-leptonic jet model for blazars – i. code description and initial results," *Monthly Notices of the Royal Astronomical Society*, vol. 512, no. 3, p. 3948–3971, 2022.

[13] W. Atwood, A. A. Abdo, M. Ackermann, W. Althouse, B. Anderson, M. Axelsson, L. Baldini, J. Ballet, D. Band, G. Barbiellini, *et al.*, "The large area telescope on the Fermi gamma-ray space telescope mission," *The Astrophysical Journal*, vol. 697, no. 2, p. 1071, 2009.

[14] T. Gaisser and A. Karle, eds., *Neutrino Astronomy: current status, future prospects*, vol. 1. World Scientific Publishing, 2017.

[15] G. Ghisellini, "The blazar sequence 2.0," *Galaxies*, vol. 4, no. 4, p. 36, 2016.

[16] B. Rani, M. Petropoulou, H. Zhang, F. D'Ammando, J. Finke, M. Baring, M. Böttcher, S. Dimitrakoudis, Z. Gan, D. Giannios, D. H. Hartmann, T. P. Krichbaum, A. P. Marscher, A. Mastichiadis, K. Nalewajko, R. Ojha, D. Paneque, C. Shrader, L. Sironi, and A. Tchekh, "Multi-Physics of AGN Jets in the Multi-Messenger era," *American Astronomical Society*, vol. 51, p. 92, May 2019. Astro2020: Decadal Survey on Astronomy and Astrophysics.

[17] T. I. Collaboration, Fermi-LAT, MAGIC, AGILE, ASAS-SN, HAWC, H.E.S.S., INTEGRAL, Kanata, Kiso, Kapteyn, L. Telescope, Subaru, Swift/NuSTAR, VERITAS, and V.-. teams, "Multimessenger observations of a flaring blazar coincident with high-energy neutrino IceCube-170922A," *Science*, vol. 361, July 2018.

[18] A. A. Zdziarski and M. Boettcher, "Hadronic models of blazars require a change of the accretion paradigm," *Monthly Notices of the Royal Astronomical Society: Letters*, vol. 450, pp. L21–L25, June 2015.

[19] F. D'Ammando, C. M. Raiteri, M. Villata, J. A. Acosta-Pulido, I. Agudo, A. A. Arkharov, R. Bachev, G. V. Baida, E. Benítez, G. A. Borman, W. Boschin,

V. Bozhilov, M. S. Butuzova, P. Calcidese, M. I. Carnerero, D. Carosati, C. Casadio, N. Castro-Segura, W.-P. Chen, G. Damljanovic, A. Di Paola, J. Echevarría, N. V. Efimova, S. A. Ehgamberdiev, C. Espinosa, A. Fuentes, A. Giunta, J. L. Gómez, T. S. Grishina, M. A. Gurwell, D. Hiriart, H. Jermak, B. Jordan, S. G. Jorstad, M. Joshi, G. N. Kimeridze, E. N. Kopatskaya, K. Kuratov, O. M. Kurtanidze, S. O. Kurtanidze, A. Lähteenmäki, V. M. Larionov, E. G. Larionova, L. V. Larionova, C. Lázaro, C. S. Lin, M. P. Malmrose, A. P. Marscher, K. Matsumoto, B. McBreen, R. Michel, B. Mihov, M. Minev, D. O. Mirzaqulov, S. N. Molina, J. W. Moody, D. A. Morozova, S. V. Nazarov, A. A. Nikiforova, M. G. Nikolashvili, J. M. Ohlert, N. Okhmat, E. Ovcharov, F. Pinna, T. A. Polakis, C. Protasio, T. Pursimo, F. J. Redondo-Lorenzo, N. Rizzi, G. Rodriguez-Coira, K. Sadakane, A. C. Sadun, M. R. Samal, S. S. Savchenko, E. Semkov, L. Sigua, B. A. Skiff, L. Slavcheva-Mihova, P. S. Smith, I. A. Steele, A. Strigachev, J. Tammi, C. Thum, M. Tornikoski, Y. V. Troitskaya, I. S. Troitsky, A. A. Vasilyev, O. Vince, (the WEBT Collaboration), T. Hovatta, S. Kiehlmann, W. Max-Moerbeck, A. C. S. Readhead, R. Reeves, T. J. Pearson, (the OVRO Team), T. Mufakharov, Y. V. Sotnikova, and M. G. Mingaliev, "Investigating the multiwavelength behaviour of the flat spectrum radio quasar CTA 102 during 2013–2017," *Monthly Notices of the Royal Astronomical Society*, vol. 490, pp. 5300–5316, 10 2019.

[20] K. Kreter, M. Kadler, F. Krauss, K. Mannheim, S. Buson, R. Ojha, J. Wilms, and M. Boettcher, "On The Detection Potential Of Blazar Flares For Current Neutrino Telescopes," *The Astrophysical Journal*, vol. 902, October 2020.

[21] M. Boettcher, "Modeling the Emission Processes in Blazars," *Astrophys Space Sci*, vol. 309, p. 95–104, April 2007.

[22] M. Boettcher, A. Reimer, K. Sweeney2, and A. Prakash, "Leptonic and Hadronic Modeling of Fermi-Detected Blazars," *The Astrophysical Journal*, vol. 768, p. 54, April 2013.

[23] M. Boettcher, "Progress in Multiwavelength and Multi-Messenger Observations of Blazars and Theoretical Challenges," *Galaxies*, vol. 7, January 2019.

[24] J. H. Fan, "Relation between bl lacertae objects and flat-spectrum radio quasars," *The Astrophysical Journal*, vol. 585, no. 1, 2003.

[25] M. Zacharias, "Studying the influence of external photon fields on blazar spectra

using a one-zone hadro-leptonic time-dependent model," *Physics*, vol. 3, no. 4, p. 1098–1111, 2021.

[26] M. Zacharias, "Exploring the evolution of the particle distribution and the cascade in a moving, expanding emission region in blazar jet," *Astronomy and Astrophysics*, 2022.

[27] A. Neronov and M. Ribordy, "Icecube sensitivity for neutrino flux from fermi blazars in quiescent states," *Physical Review D*, vol. 80, no. 8, p. 083008, 2009.

[28] S. Priya, R. Prince, A. Agarwal, D. Bose, A. Özdönmez, and E. Ege, "Multiwavelength temporal and spectral analysis of Blazar S5 1803+ 78," *Monthly Notices of the Royal Astronomical Society*, vol. 513, no. 2, pp. 2239–2251, 2022.

[29] L. Foschini, E. Pian, L. Maraschi, C. M. Raiteri, F. Tavecchio, G. Ghisellini, G. Tosti, G. Malaguti, and G. D. Cocco, "A short hard X-ray flare from the blazar NRAO 530 observed by INTEGRAL," *Astronomy and Astrophysics*, vol. 450, pp. 77–81, 2006.

[30] G. Wang, J. Fan, H. Xiao, and J. Cai, "Variability and Spectral Behavior of Gamma-Ray Flares of 3C 279," *Publications of the Astronomical Society of the Pacific*, vol. 134, no. 1040, p. 104101, 2022.

[31] V. S. Paliya, M. Böttcher, M. Gurwell, and C. S. Stalin, "On the origin of gamma-ray flares from bright fermi blazars," *The Astrophysical Journal Supplement Series*, vol. 257, p. 37, nov 2021.

[32] A. Bettini, *Introduction to elementary particle physics*. Cambridge University Press, 2014.

[33] J. G. Linhart, *Cherenkov radiation*. British Thomson-Houston, 1955.

[34] L. Wan, "Simulation and sensitivity studies for solar neutrinos at jinping," *Solar Neutrinos*, 2019.

[35] Z.-Y. Wang, X.-Y. Wang, and J.-F. Wang, "Neutrinos from gamma-ray bursts: Propagation of cosmic rays in their host galaxies," *The Astrophysical Journal*, vol. 803, no. 1, 2015.

[36] L. Di Lella and C. Rubbia, "The Discovery of the W and Z Particles," *Adv. Ser. Dir. High Energy Phys.*, vol. 23, pp. 137–163, 2015.

[37] J. Cao and M. He, "Neutrino oscillation: discovery and perspectives," *Science Bulletin*, vol. 61, pp. 48–51, 2016.

[38] O. Pisanti, "Astrophysical neutrinos: theory," *Journal of Physics: Conference Series*, vol. 1263, p. 012004, jun 2019.

[39] "Constraint on the matter–antimatter symmetry-violating phase in neutrino oscillations," *Nature*, vol. 580, no. 7803, pp. 339–344, 2020.

[40] K. Nakamura, "HYPER-KAMIOKANDE — A Next Generation Water Cherenkov Detector," *International Journal of Modern Physics A*, vol. 18, no. 22, pp. 4053–4063, 2003.

[41] K. Collaboration *et al.*, "KM3NeT 2.0 Letter of Intent for ARCA and ORCA," *J. Phys. G: Nucl. Part. Phys*, vol. 43, p. 084001, 2016.

[42] M. G. Aartsen, R. Abbasi, M. Ackermann, J. Adams, J. Aguilar, M. Ahlers, M. Ahrens, C. Alispach, P. Allison, N. Amin, *et al.*, "Icecube-gen2: the window to the extreme universe," *Journal of Physics G: Nuclear and Particle Physics*, vol. 48, no. 6, p. 060501, 2021.

[43] T. K. Collaboration, "Sensitivity of the KM3NeT/ARCA neutrino telescope to point-like neutrino sources," *Journal of Astroparticle Physics*, vol. 111, pp. 100–110, September 2019.

[44] I. Collaboration*†, R. Abbasi, M. Ackermann, J. Adams, J. Aguilar, M. Ahlers, M. Ahrens, J. Alameddine, C. Alispach, A. Alves Jr, *et al.*, "Evidence for neutrino emission from the nearby active galaxy NGC 1068," *Science*, vol. 378, no. 6619, pp. 538–543, 2022.

[45] A. Dolmi, S. Bourret, and A. Quinn, "Particle Physics with ORCA," *EPJ Web of Conferences*, vol. 207, p. 4, May 2019.

[46] S. H. Haddock, M. A. Moline, and J. F. Case, "Bioluminescence in the sea," *Annual review of marine science*, vol. 2, pp. 443–493, 2010.

[47] T. K. Collaboration, "Comparison of the measured atmospheric muon flux with Monte Carlo simulations for the first KM3NeT detection units," *Proceedings of Science*, vol. 358 - International Cosmic Rays Conference, p. 7, July 2019.

[48] G. Helou, B. F. Madore, M. Schmitz, X. Wu, H. G. Corwin, C. LaGue, J. Bennett, and H. Sun, "The nasa/ipac extragalactic database," *Astrophysics and Space Science Library*, p. 95–113, 1995.

[49] M. Honda, T. Kajita, K. Kasahara, S. Midorikawa, and T. Sanuki, "Calculation of atmospheric neutrino flux using the interaction model calibrated with atmospheric muon data," *Physical Review D*, vol. 75, no. 4, 2007.

[50] R. Enberg, M. H. Reno, and I. Sarcevic, "Prompt neutrino fluxes from atmospheric charm," *Physical Review D*, vol. 78, no. 4, 2008.

[51] T. K. Gaisser, "Spectrum of cosmic-ray nucleons, kaon production, and the atmospheric muon charge ratio," *Astroparticle Physics*, vol. 35, no. 12, pp. 801–806, 2012.

[52] K. Melis, A. Heijboer, and M. de Jong, "KM3NeT/ARCA event reconstruction algorithms," in *Proceedings, 35th International Cosmic Ray Conference (ICRC2017)*, pp. 76–78, 2017.

[53] G. C. HILL, J. HODGES, B. HUGHEY, A. KARLE, and M. STAMATIKOS, "Examining the balance between optimising an analysis for best limit setting and best discovery potential," *Statistical Problems in Particle Physics, Astrophysics and Cosmology*, 2006.

[54] G. J. Feldman and R. D. Cousins, "Unified approach to the classical statistical analysis of small signals," *Physical Review D*, vol. 57, no. 7, p. 3873–3889, 1998.